Physics – Uspekhi **42** (11) 1139 – 1166 (1999)

REVIEWS OF TOPICAL PROBLEMS PACS numbers: **41.75.–i**, **61.80.–x**, **81.15.–z**, **81.40.–z**

Metal modification by high-power pulsed particle beams

V I Boĭko, A N Valyaev, A D Pogrebnyak

Contents

Abstract. The state of the art in the modification of iron, steel, and titanium alloys and some metal multilayers by medium intensity ($10^6 - 10^9$ W cm^{-2}) pulsed electron and ion beams is summarized, including the contribution from the authors. Many of the processes that determine the defect structure and its properties are described and such problems as the formation of elastoplastic and shock waves, mixing of multilayers, thin film deposition, and nanophase powder synthesis are discussed. The high potential of particle beam technology — in particular, for improving the operating characteristics of materials — has been demonstrated amply by research centers worldwide.

V I Boĭko Tomsk Polytechnical University,
634004 Tomsk, Russian Federation
Tel. (7-8382) 41 89 02. Fax (7-8382) 41 89 01
E-mail: boiko@phtd.tpu.ru
A N Valyaev East Kazakhstan Technical University,
ul. Lugovaya 19, 492022 Ust'-Kamenogorsk, Kazakhstan
Tel. (7-3232) 40 68 63. Fax (7-3232) 26 89 31
E-mail: root@vktu.iatp.kz
A D Pogrebnyak Sumy Institute for Surface Modification,
P.O. Box 163, prosp. Shevchenko 17, 244034 Sumy, Ukraine
Tel. (38-0542) 22 03 38. Fax (38-0542) 27 50 02
E-mail: pogreb@diskret.sumy.ua

Received 24 April 1998, revised 27 May 1999
Uspekhi Fizicheskikh Nauk **169** (11) 1243 – 1271 (1999)
Translated by E Yankovsky; edited by S N Gorin

1. Introduction

The emergence in the last few decades of optical quantum generators and accelerators of high-current electron beams (HEB) and high-power ion beams (HIB) has created the unique possibility of establishing new ways of acting on materials by concentrated energy fluxes. In contrast to the traditional methods such as impact-wave loading and quenching and annealing of steel, the beam approach incorporates simultaneous radiative, thermal, and mechanical action. In this realm, unique effects have been detected, such as the condensation of excitons in semiconductors subjected to laser radiation [1, 2], brittle fracture of all types of solids under HEB [3 – 8], surface [9 – 18] and bulk [9 – 15, 19 – 21] strain hardening of metals irradiated with HIB, generation of elastic [14, 15, 22 – 27] and shock [5, 15, 28] waves, and intensive ablation of matter in the plasma state under HEB [4] and HIB [16 – 18, 29 – 37]. Most of these phenomena are nonlinear and can be observed at intensities and fluences exceeding certain critical values. Radiation-stimulated processes have a complicated physical nature related to the specific features of the transformation and accumulation of the absorbed energy in the event of superdense excitations of the electronic and atomic subsystems of solids [7, 38]. This facilitated the development of new fundamental directions in the physics of high energy densities, including the solution of the problem of controlled thermonuclear fusion [39, 40].

New directions evolved in radiative materials science, directions related to the solution of applied problems of nuclear power engineering, the aerospace industry, mechanical engineering, microelectronics, etc. It was found that the

traditional chemicothermal methods of processing materials could not solve the new problems and had practically used up their potential, while ion implantation did not always yield the necessary results. Laser light was found to be highly effective, a fact reflected, e.g., in Refs [41 – 46]. However, laser beams have moderate efficiency and are characterized by small processing areas, high production costs, and in some cases a high reflectivity from the target surface.

Now, when for well-known reasons the financing of R&D in beam weapons has been cut considerably worldwide and in many countries conversion programs have been developed, the need emerged to use the operating high-current accelerators for new goals and problems. Such accelerators are being developed for specific applications [47], and their main parameters are the beam composition, the particle energy, and the intensity and duration of the irradiation. It is the values of these parameters, the conditions of irradiation, and the properties of the material that determine the rates of heating, cooling, melting, and evaporation of the material, the ablation of the surface layers, the development of thermal stresses, and the generation of elastic and shock waves. The above processes determine the modified properties of materials not only in the surface layers but also in the bulk at depths that exceed the projected particle range by several orders of magnitude, i.e., long-range effects arise.

Low-energy (up to several tens of keV) and high-energy (several MeV) HEBs with pulse lengths varied from 10^{-8} to 10^{-6} s, current densities up to several kA cm^{-2}, and fluences up to several hundred J cm^{-2} per pulse are used to modify materials. Beams of light ions (such as ions of hydrogen, carbon, and nitrogen) are effective in the treatment of materials since, first, they are easier to produce and, second, the ranges of light ions are much longer than those of heavy ions. The parameters of the ion beams are as follows: the energy is 0.1 to 2 MeV, the current in a pulse varies from 5 to 50 kA, and the intensities and fluences are from 10^7 to 10^{10} W cm^{-2} and from 1 to 100 J cm^{-2} per pulse, respectively. Such beams cause rapid heating and cooling in the surface layers of metals with rates from 10^8 to 10^{11} K s^{-1} and minimum heat removal. These heating and cooling processes, in conjunction with large spatial temperature gradients, $10^6 - 10^7$ K cm^{-1}, lead to unique modifications of the properties. The fact that the ranges of the electrons and ions in metals differ by several orders of magnitude (at equal energies) determines the specific features and in some cases the difference of the observed macrocharacteristics.

Both HEBs and HIBs have certain advantages over laser beams: much higher efficiencies, lower cost of beam generation per unit energy, larger treatment areas (up to 10^3 cm^2), and higher degrees of absorption in all materials. Beams of light ions are capable of modifying the properties at depths 10 to 20 times greater than the implantation of heavy ions does and with fluences that are several orders of magnitude smaller. The progress in employing HEBs and HIBs has stimulated the development of new large-scale commercial technologies. A new technology, known as Intense Pulsed Ion Beam Evaporation (IBE), has been developed in Japan and is used to produce thin films in the electronic and optical industries and to diagnose intense radiations. Another example is the program of Ion Beam Surface Treatment (IBEST), which emerged in the USA.

At present the areas in which HIBs and HEBs are used are as follows: the production of superdense plasma for controlled thermonuclear fusion [39, 40]; the implantation and annealing of semiconductors [47 – 49]; the modification of strength [9 – 15, 19 – 22, 41 – 47], tribological [10, 50 – 52], and corrosion-resistance [50, 53, 54] properties of metals and alloys; the synthesis of new composite materials, including metastable phases and compounds [11, 55, 56]; the production of thin films and coatings with a given structure and properties via ablation-plasma deposition [16 – 18]; cleaning [56 – 58], polishing [56], and glossing [56] of surfaces; synthesis of nanophase powders [16, 18]; and the destruction and cutting of solid materials [4 – 8, 59]. Realization of the necessary technology is achieved by selecting the proper intensity and duration of irradiation.

The plan of the present review is as follows. Section 2 discusses the main results of studies of structural and phase transitions in α-Fe irradiated with HEBs. In Section 3 we consider similar data obtained upon irradiation with HIBs. There, we demonstrate the important role that the generated shock wave plays in the transitions at large depths and propose a kinetic model of strain hardening. The results of experimental studies of mixing processes in the event of HEB irradiation of a double-layer metallic system in the form of a thin high-melting Mo or Ta film on an iron substrate are discussed in Section 4. Section 5 analyzes the possible models of mass transport. The behavior of matter in the presence of elastoplastic waves generated by intense irradiation is described in Section 6. The technology of manufacturing thin films by depositing the ablation plasma formed in the process of irradiation is discussed in Section 7. There we show the possibility of synthesizing thin films with special properties and ultradisperse (nanosized) powders. Some typical examples of modifications of the operating characteristics of metals, alloys, and products from these metals and alloys after beam processing are described in Section 8. Finally, in the Conclusion we note that the topics discussed in this review demonstrate good prospects for using high-power pulsed beams to modify materials.

The list of references is certainly incomplete, but we believe that it reflects the most important works of the researchers in the topics covered in the review.

2. Structural and phase transitions in α-Fe irradiated with a high-current pulsed electron beam

At the beginning, HEBs were used to anneal defects in implanted layers of semiconductors [55, 60, 61]. However, this approach did not become widespread because of the inhomogeneities in the density of the plasma obtained via explosive-emission cathodes and also due to the appearance of high thermal stresses in the surface layers, stresses that generate micro- and macrocracks. Later HEBs were used to modify metals. Structural and phase transitions in the surface layers of metals are determined by the initial state of the material, the dynamics of the temperature fields and thermal-stress fields in the region in which the beam is absorbed and in the adjoining high-temperature zone, which is known as the thermal-affected zone, or TAZ. At large depths, these transitions are related to the effect of elastic, elastoplastic, and shock waves. The nature of defect formation in these two areas is different; therefore, we consider each case separately.

2.1 Modification in the thermal-affected zone

Hewett et al. [48], Ivanov et al. [49 – 51], and Lykov et al. [52] studied transitions in pure (10^{-4} wt. % nitrogen) α-Fe with an

average grain size of 10 μm along the thermal-affected zone after irradiation with a low-energy HEB (LHEB) with the following parameters: pulse length $\tau_p = 0.8$ μm, electron energy 10–20 keV, and fluence $\Phi = 2-2.5$ J cm^{-2} per pulse. The number of pulses varied from 1 to 300 with a frequency of 0.1 Hz. The surface was found to contain remelted areas of about 30 μm in size, and traces of plastic deformation caused by thermal stresses (the nature of these stresses corresponds to high-temperature deformation, as in ordinary pulsed heating) were clearly visible in all grains. In the surface layer (< 5 μm), recrystallization centers 2–5 μm in size appear in the initial grains, primarily at the boundaries of these grains. At the same time, sections with a misoriented cellular dislocation structure were observed in one grain, while inside the initial grains, notwithstanding the strong deformation, there were practically no dislocations, which indicates that high-temperature annealing occurred after deformation. Hence, in this layer plastic deformation was accompanied by primary recrystallization. At depths larger than 5 μm, heating did not have a noticeable effect on the dislocation structure characteristic of impact-wave loading. The dislocation density was found to decrease monotonically with increasing depth. This behavior was retained as the number of pulses increased, except that the degree of plastic deformation was increasing. Comparison of the dislocation structures obtained by uniaxial stretching and by applying a LHEB (300 pulses) has shown that at depths of 20–50 μm the degree of plastic deformation was 2–5%.

The variations in the grain and dislocation structures with depth are due to the rapid heating of the surface layers to the melting point and above, followed by rapid cooling due to heat removal, and also due to the effect of stress waves [51, 52]. Let us analyze the conditions during the formation of the microstructure over the depth. Figure 1 depicts the time dependence of temperature at different depths for an irradiation fluence $\Phi = 2.2$ J cm^{-2} per pulse. The surface layer that melts has a thickness of about 0.2 μm. The rates of heating of the surface immediately before melting and the rate of cooling layer immediately after the solidification is completed are 5×10^9 and 10^{10} K s^{-1}, respectively. Outside

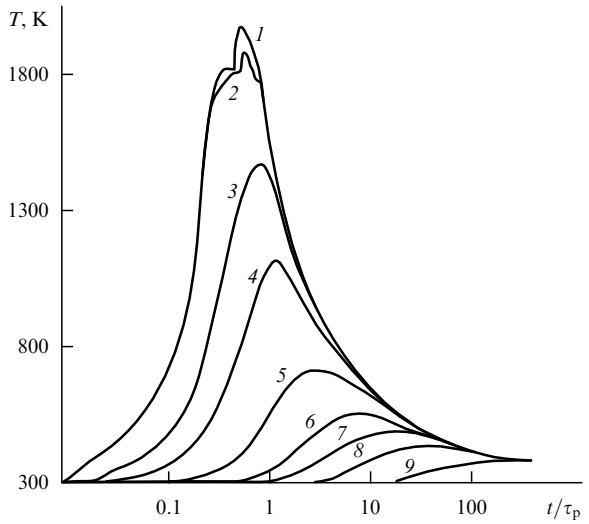

Figure 1. Time dependence of temperature at different depths x measured from the surface of α-Fe irradiated by a LHEB (10–20 keV, 0.8 μs, 2.2 J cm^{-2} per pulse): *1*, $x = 0.2$; *2*, 0.2; *3*, 1; *4*, 2; *5*, 5; *6*, 10; *7*, 16; *8*, 20; and *9*, 25 μm.

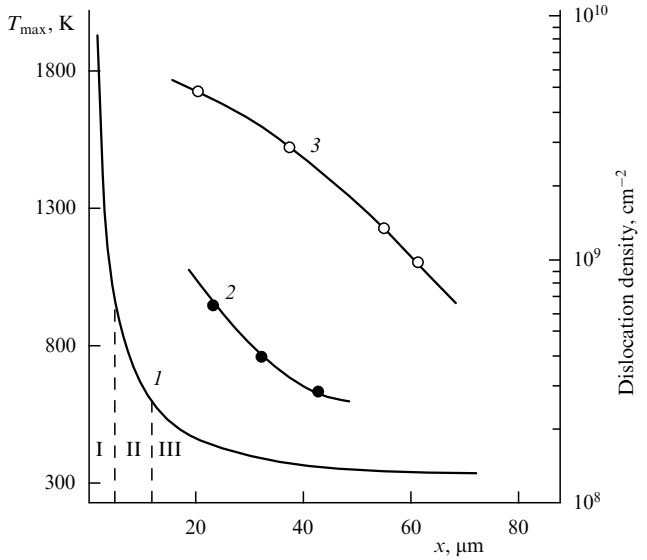

Figure 2. Maximum temperature (curve *1*) and dislocation density as functions of the depth in α-Fe after LHEB irradiation (10–20 keV, 0.8 μs, 2.2 J cm^{-2} per pulse) with the number of pulses being $N = 5$ (curve *2*) and $N = 300$ (curve *3*).

the energy-deposition zone (> 2 μm), the maximum temperature (T_{max}) was reached after the pulse had ceased (the reason for this is that the rate of propagation of heat is finite). The heating and cooling rates and the temperature T_{max} reached at a given point were found to decrease with increasing depth (curve *1* in Fig. 2). It was found that by the time the pulse ended the thickness of the heated layer was about 15 μm (see Fig. 1); after the irradiation was terminated, the thickness increased to 70 μm due to redistribution of heat. It took about 10^{-3} s for the temperature of the layer to drop to room temperature.

Another factor that affects the microstructure of iron is the stress wave generated in the surface layer with a thickness of about 1 μm (the range of the electrons of the beam). As shown by Ivanov et al. [51], the wave is bipolar and consists of pulses of compression and tension $\sim 10^{-6}$ s long. Estimates have shown that the wave's amplitude (1–8.5 GPa) is much larger than the dynamic yield strength of iron. This wave forms a dislocation substructure, and due to wave attenuation the dislocation density monotonically decreases with increasing depth.

The wavefront of the stress wave outstrips the wavefront of the thermal wave substantially. Hence, plastic deformation is accompanied by recovery processes, one of which is recrystallization. Let us compare the results of structural analysis with those of calculations of thermal fields. Three regions are clearly visible in the diagram representing the dependence of T_{max} on depth (see curve *1* in Fig. 2). In the first region ($x < 5$ μm), $T_{max} \geqslant 0.4T_m$ (for iron the recrystallization temperature amounts to $0.4T_m \sim 750$ K, where $T_m = 1810$ K is the melting point of Fe). Hence, in this region recrystallization and intense redistribution of dislocations can occur, which reduce the dislocation density. This conclusion is in good agreement with the experimental data. Such an approach makes it possible to study time–temperature processes in the initial stages of recrystallization. For instance, calculations show that it takes $\sim 5 \times 10^{-6}$ s for the recrystallization nuclei to grow. Hence, the rate of this growth is 0.4–1 m s^{-1}. The second region lies at a depth of 5–12 μm, where the temperature reaches 500–700 K. At such a

temperature, a redistribution of dislocations can occur without their density decreasing significantly, with the result that the recrystallization probability is low. At large depths (region III), there is no dislocation redistribution, since here the temperature is much lower than the recrystallization temperature [53]. Indeed, in this region, as the experimental data show (see curves *2* and *3* in Fig. 2), the dislocation density decreases monotonically with increasing depth, i.e., the effect of temperature is insignificant. Thus, the nature of the structural changes with depth in irradiated α-Fe is determined by the plastic deformation caused by stress waves and subsequent recrystallization caused by the propagation of a heat wave.

2.2 Changes in the defect structure and mechanical properties of α-Fe quenched from the liquid state

Of interest here is the microstructure of the surface layer roughly 1 μm thick in which substantial thermoelastic stresses arise and simultaneously whose temperature is high. Due to the rapid quenching from the melt, formation of vacancy-type point defects is possible in such a layer [54]. The methods of Rutherford back scattering (RBS), electron–positron annihilation (EPA), secondary-ion mass spectroscopy (SIMS), and transmission electron microscopy (TEM) were used (see Refs [62, 63]) to study the effect of the defect structure of α-Fe produced by irradiation on the variation of the microhardness and wear of the sample. The results were analyzed by calculating thermal fields.

Recrystallized samples containing carbon, nitrogen, and oxygen with concentrations < 0.008, < 0.0014, and < 0.0001 wt. % with fine (several tens of micrometers) and coarse (2–4 mm) grains were irradiated with a LHEB. The minimum fluence corresponded to the threshold value at which a pattern characteristic of a solidified melt was formed at the surface. The EPA method used $^{22}Na(\beta^+, \gamma)$ as a source of positrons, with a lifetime described by two components $\tau_1 = 250$ ps and $\tau_2 = 450$ ps with intensities $I_1 = 6.2\%$ and $I_2 = 2.5\%$, respectively. At $\Phi = 3.3$ J cm^{-2} per pulse, the positrons were trapped by defects, in which their lifetime also had two components, $\tau_1 = 108$ ps and $\tau_2 = 195 \pm 3$ ps. According to the theoretical research done by Puska and Nieminen [64] and the experiments conducted by Markov et al. [53], the value of τ_2 corresponds to the lifetime of a positron trapped by a divacancy, while τ_1 is the lifetime of a positron localized in a pure 'defect-free' material. An increase in Φ to 4.2 J cm^{-2} per pulse changes the values of τ and I: $\tau_1 = 116$ ps and $\tau_2 = 225 \pm 4$ ps, with the increase in τ_2 accompanied by a decrease in I_2, which points to a decrease in the concentration of vacancy clusters. Allowing for the data of Lykov et al. [52], we can expect that at $\Phi = 4.2$ J cm^{-2} per pulse larger defects are formed (clusters consisting of three or more vacancies). The value $\tau_1 = 116$ ps exceeds the lifetime of a positron in 'defect-free' iron (108 ps). Apparently this value includes the lifetime of positrons localized at dislocations, which in comparison to vacancies and vacancy clusters are shallower traps. The value $\tau_2' = 165 \pm 2$ ps was obtained in Ref. [63] by fixing τ_1' at 108 ps. Thus, the positrons annihilating in the bulk have a lifetime $\tau_1' = 108$ ps, while the value $\tau_2' = 165 \pm 2$ ps corresponds to positrons trapped by dislocations. These conclusions are in good agreement with the well-known data. Note that the information extracted by this method originates in a layer that is 0.1 to 40 μm thick.

Figure 3 displays the energy spectra of channeled helium ions $^4He^{++}$ measured for an oriented grain in the surface layer

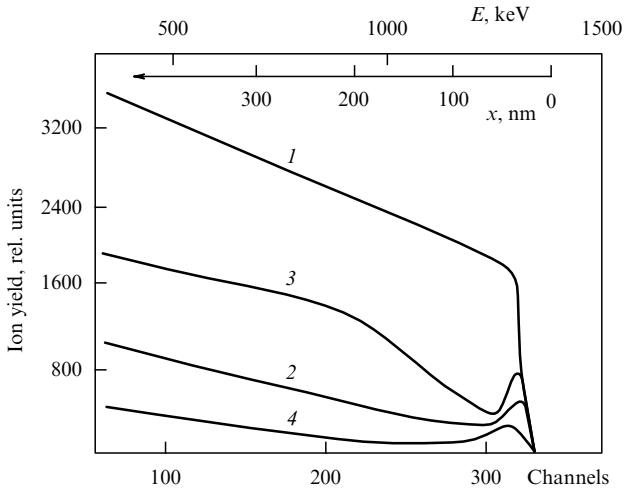

Figure 3. Spectra of back scattering (*I*) and of channeling of helium ions (with an energy of 2 MeV) in the [100] direction for iron grains oriented on the (100) plane: *1*, the initial sample (unoriented crystal); *2*, the initial sample with a coarse grain (~ 4 mm) of (100) orientation; *3* and *4*, sample after irradiation by LHEBs with fluences amounting to 3.3 and 5.2 J cm^{-2} per pulse, respectively ($\tau_p = 0.8$ μs).

of α-Fe before and after irradiation. In the initial state, α-Fe has an imperfect crystal lattice, a fact corroborated by the high yield of scattered ions $^4He^{++}$. When a fluence of 3.3 J cm^{-2} per pulse is applied to the sample, the yield increases, i.e., the degree of order in the crystal lattice decreases as a result of formation of defects in the crystal (primarily interstitial defects). The curve corresponding to this regime has two sections with different slopes and, naturally, different concentrations of defects [63]. In addition to a surface peak reflecting the presence of imperfections at depths of 50 to 200 nm, a decrease in crystallinity was observed related to the formation of interstitial-atom clusters, loops, and dislocations. A similar spectrum behavior in the form of 'erosion' was observed by Verigin et al. [65] and was explained by the formation of edge and screw dislocations. It was found that inside the modified layer (due to melting), beginning at a depth of 200 nm, a region is formed with an almost constant defect concentration. At fluences higher than 3.3 J cm^{-2} per pulse, the yield of the backscattered ions was found to decrease, which suggests a higher degree of order of the crystal lattice (or partial annealing of defects in comparison with the regime with 3.3 J cm^{-2} per pulse).

Figure 4 depicts curves representing the dependence of the *S* parameter of Doppler broadening of annihilation peaks on the energy of the probing positron beam (or the layer depth on the upper scale) for irradiated α-Fe (here $S = N(0)/N(10)$, with $N(0)$ and $N(10)$ being the counting rates at the maxima of the curves of the angular distribution of annihilation photons for angles equal to 0 and 10 mrad). Irradiation with a fluence of 2.3 J cm^{-2} per pulse generated, as a result of quenching, vacancy type defects (clusters of vacancies, divacancies, trivacancies, etc.) beginning at a depth of 100 nm up to the entire depth of the layer being analyzed (1020 nm). The maximum increase in the *S* parameter, found to correspond to a fluence of 4.2 J cm^{-2} per pulse, was due to the increase in the concentration of point defects and the generation of dislocations (these conclusions follow from the results of positron-lifetime measurements and TEM studies). An increase in fluence to 5.2 J cm^{-2} per pulse was found to

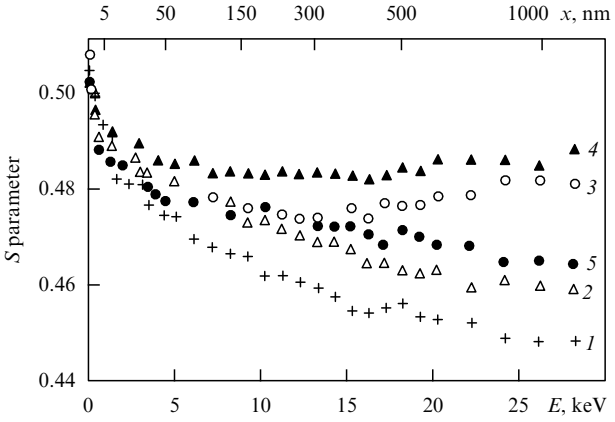

Figure 4. Dependence of the *S* parameter on the positron energy for pre-annealed samples (at different temperatures) of α-Fe after LHEB irradiation in different regimes: *1*, 910 °C, prior to irradiation; *2*, 910 °C, 2.3 J cm^{-2} per pulse; *3*, 840 °C, 2.3 J cm^{-2} per pulse; *4*, 910 °C, 4.2 J cm^{-2} per pulse; and *5*, 840 °C, 4.2 J cm^{-2} per pulse.

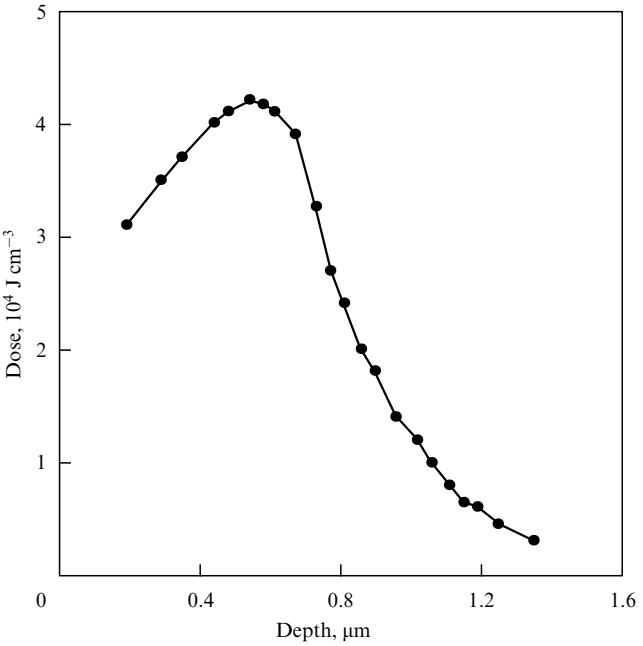

Figure 5. Distribution of the deposited dose in an α-Fe target irradiated using an HIB (~ 70% C^+, ~ 30% H^+, 0.4 MeV, 100 ns, and 3.3 J cm^{-2} per pulse).

lead to partial annealing of defects in comparison to the case with a fluence of 4.2 J cm^{-2} per pulse, while the *S* parameter decreased in a surface layer at depths of up to 250 nm (which correlates with the RBS results). However, already at a depth of approximately 1 μm, even in the event of thermal annealing at 800 °C, defects remained to which positrons were sensitive. SIMS analysis of these annealed samples showed that the concentration of V was approximately ten times higher than the concentrations of W and Mo [63]. Hence, the researchers suggested that the positrons annihilate at impurity complexes including vanadium atoms.

Thus, it has been established that the changes that occur in the thermal-affected zone are due to changes in the grain and dislocation structures. The high rates of the heating and cooling of the surface layers and the subsequent recrystallization processes form surface layers with different types of defects and different defect concentrations. In the surface layer (< 1 μm), the additional effect of thermoelastic stresses forms point defects and complexes of such defects (clusters of interstitial defects and screw and edge dislocations), which produce a microstructure that improves the mechanical and tribological properties of iron [62, 63].

3. Modifications of the structure and mechanical properties of metals via high-power pulsed ion beams

The experiments conducted in the late 1980s and early 1990s by the authors of Refs [9, 10, 66, 67] revealed that in aluminum, copper, and tungsten irradiated with high-power ion beams with intensities $\geqslant 10^8$ W cm^{-2}, in addition to the well-known enhancement of microhardness, an additional peak of microhardness is formed at depths much larger than the ion range, i.e., a long-range effect manifests itself. Hence, the next problem was to study the effect of the laws governing the development of a defect structure on the formation and localization of this peak. Irradiation of the samples was carried out on a TONUS accelerator with the following parameters: the beam consisted of roughly 70% C^+ and 30% H^+, the ion energy was 0.2–0.6 MeV, the pulse length was $\tau_p = 40-100$ ns, and the current density at the target surface was $j = 20-250$ A cm^{-2}; another device that was used in these experiments was a VERA accelerator (50% H^+, 50% C^+, 0.5 MeV, 100 ns, and 100–2500 A cm^{-2}). Since at *j* higher than 100 A cm^{-2} the pulse length τ_p did not vary (100 ns), $\Phi \sim j$. Calculations of the dose distribution took into account the linear ion losses with depth [68] and the percentage of the ions in the beam. The dose distribution in α-Fe is depicted in Fig. 5. Note that the depth of the irradiated region did not exceed 2 μm.

3.1 Defect formation in irradiated α-Fe and its effect on microhardness

Table 1 lists the values of the positron lifetimes τ, the point defect concentration, the dislocation density, and the microhardness measured in the surface layer (with a thickness less than 0.5 μm) of α-Fe irradiated with single pulses of an HIB. All the spectra for τ were decomposed into two components [69]. In the initial (annealed) sample, $\tau = 114 \pm 2$ ps, which is close to Puska and Nieminen's data [64], where in defect-free α-Fe the value of τ_1 is 110 ± 2 ps (positrons annihilate mainly with $3d^64s^2$ electrons [70]). At $j > 100$ A cm^{-2}, melting, evaporation, and sublimation occur at the sample's surface, with the result that thermomechanical stresses arise. Estimates of these stresses in the model developed in Ref. [71] yield 10^8-10^{10} Pa, which is sufficient for plastic deformation to occur.

Measurements of the recoil impulse made with a gravity pendulum and aperiodic detectors and the determination by the gravimetric method of the target mass loss yielded the amplitude of the shock wave (SW) varying from 2 to 14 GPa, depending on the fluence [66]. Some researchers, whose results can be found in the review articles of Mogilevsky [72] and Murr and Gray [73], established by experiments that such SW cause intensive defect formation. Indeed, EPA analysis and electron-microscopic observations revealed the formation of structures with a large density of dislocations, dislocation loops, vacancy clusters, and vacancy complexes. Positrons were found to be effectively trapped by vacancy

Table 1. Positron lifetimes, point defect concentrations n_i, dislocation densities n_d, and the microhardness H in the surface layer of α-Fe (< 0.5 μm) irradiated by single pulses of an HIB.

j, À cm^{-2}	τ_1, ps	I_1, %	τ_2, ps	I_2, %	H, MPa	n_i, 10^{18} cm^{-3}	n_d, 10^9 cm^{-2}
—	112	100	—	—	760 ± 20	—	0.5
60	112 ± 1	88.2 ± 2.7	193 ± 10	11.8 ± 2.7	880 ± 35	0.136	2.7
150	109 ± 2	76.4 ± 3.0	192 ± 2	23.6 ± 3.0	920 ± 35	0.285	4.0
250	108 ± 2	72.3 ± 3.7	193 ± 4	27.7 ± 3.7	935 ± 30	0.324	4.9
600	108 ± 2	64.6 ± 3.0	191 ± 4	35.4 ± 3.0	1120 ± 65	0.479	9.7
1000	109 ± 1	60.2 ± 2.8	192 ± 2	39.8 ± 2.8	1210 ± 60	0.485	11.05
1500	108 ± 3	52.7 ± 3.0	195 ± 3	47.3 ± 3.0	1230 ± 70	0.686	11.15
2000	112 ± 2	75.6 ± 2.6	221 ± 3	24.4 ± 2.6	1280 ± 65	0.452	—
2500	116 ± 3	70.5 ± 2.1	222 ± 4	29.5 ± 2.1	1350 ± 60	0.377	—

clusters, primarily divacancies, with a lifetime $\tau_2 = 192 \pm 3$ ps [64]. As j becomes larger, there is a rise in the positron trapping rate in the single-pulse regime, and sizes of the vacancy clusters change. At $j = 2500$ A cm^{-2} positrons are trapped by defects with $\tau_2 = 224 \pm 5$ ps, which, according to Puska and Nieminen [64], corresponds to trivacancies. Moreover, the value $\tau_1 = 116$ ps exceeds the lifetime of positrons annihilating in the bulk (108 ps) and incorporates the value of the lifetime of positrons localized at dislocations, which in comparison to vacancies and clusters are 'shallower' traps for positrons [74]. The value $\tau_2' = 165 \pm 2$ ps corresponds to the lifetime of positrons trapped by dislocations, a conclusion that is in good agreement with the existing data [70].

Prior to irradiation, the dislocation structure in α-Fe is represented by randomly distributed single dislocations [69, 70]. After irradiation, a dislocation structure is formed in the surface layer that is nonuniform in cross sections both perpendicular and parallel to the irradiated surface and varies from a uniform dislocation distribution to complex dislocation tangles. At $j > 200$ A cm^{-2}, the dislocation structure undergoes a substantial transformation: dislocation cells begin to form (i.e., a cellular structure is formed). The results of detailed electron-microscopic observations can be found in Ref. [69]. In the surface layer (< 5 μm), the structure contains uniformly distributed individual dislocations. At the irradiated surface, the average density of these dislocations reaches 3.6×10^9 cm^{-2}, while at a depth of 5 μm their density is 2.2×10^9 cm^{-2}. At a depth of 10 μm the dislocation structure becomes nonuniform, i.e., regions with individual dislocations and regions with a network dislocation structure are observed. Dramatic changes in the structure begin at a depth of 30 μm, where it becomes highly nonuniform. In addition to a random dislocation structure, which is represented by individual dislocations and dislocation tangles, low-angle boundaries arise, which vary from dislocation nets with a misorientation angle of roughly 1° to boundaries with a misorientation angle of 5–7°, where individual dislocations already cannot be resolved in electron-microscopic images. Beginning at a depth of 50 μm, regions with polygonized structure are observed, where low-angle grain boundaries are grouped to form extended fragments which pass through the entire initial grains of the polycrystal. The dislocation densities for all the structural components at different depths are listed in Table 2. Thus, when examining the structure of the entire modified layer (starting from the surface), the entire spectrum of point and planar defects, which are unevenly distributed over the depth, can be revealed in it.

Figure 6 depicts the current-density dependence of the average scalar dislocation density $n_d(j)$ and the microhardness $H(j)$ in a thin surface layer (< 0.5 μm) of α-Fe for a broad range of current densities, $j = 60 - 2500$ A cm^{-2}, which roughly corresponds to a variation in fluence by a factor of 40. The value of n_d at $j = 2500$ A cm^{-2} was found to increase by a factor of approximately 20 with respect to the initial value (5×10^8 cm^{-2}), while the microhardness was found to increase by a factor of two (the initial value of H amounted to roughly 700 MPa). A characteristic feature of such behavior is the strong correlation between $n_d(j)$ and $H(j)$. The distributions $n_d(x)$ and $H(x)$ over the depth of the modified layer of α-Fe obtained in two irradiation regimes (150 and 400 A cm^{-2}) were also found to correlate and had two distinct peaks (Fig. 7). The first peak is near the surface and is related to thermomechanical stresses [71, 76]. The observed slight shifts of this peak with increasing j are related primarily to the

Table 2. Dislocation densities for different dislocation structures in α-Fe irradiated by an HIB (100 ns, 5.5 J cm^{-2} per pulse).

Layer depth, μm	Dislocation density in the regions			
	with individual dislocations, 10^9 cm^{-2}	with a network structure, 10^9 cm^{-2}	with low-angle boundaries with a misorientation angle ~ 1°, 10^9 cm^{-2}	with a polygonized structure, 10^9 cm^{-2}
0	1.5	—	—	—
5	1.8	—	—	—
10	2.7	3.8	—	—
30	1.6	—	6	—
50	3.9	1.5	6	—
70	6.2	3.6	6	—
90	2.5	4.2	6	3.9
120	0.8	2.0	—	—

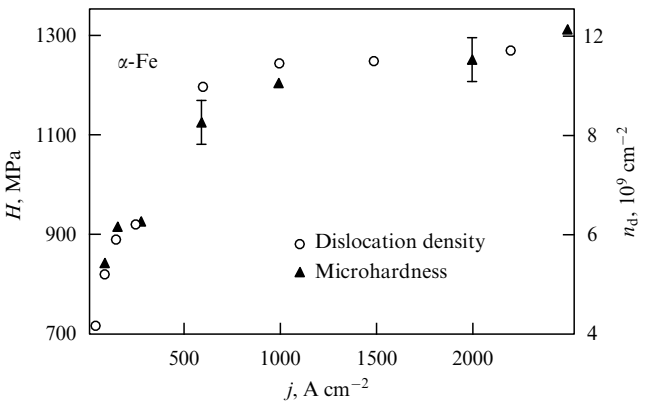

Figure 6. Variation of the average scalar dislocation density n_d and the microhardness H in the surface layer (< 0.5 μm) of α-Fe as a function of the HIB current density j.

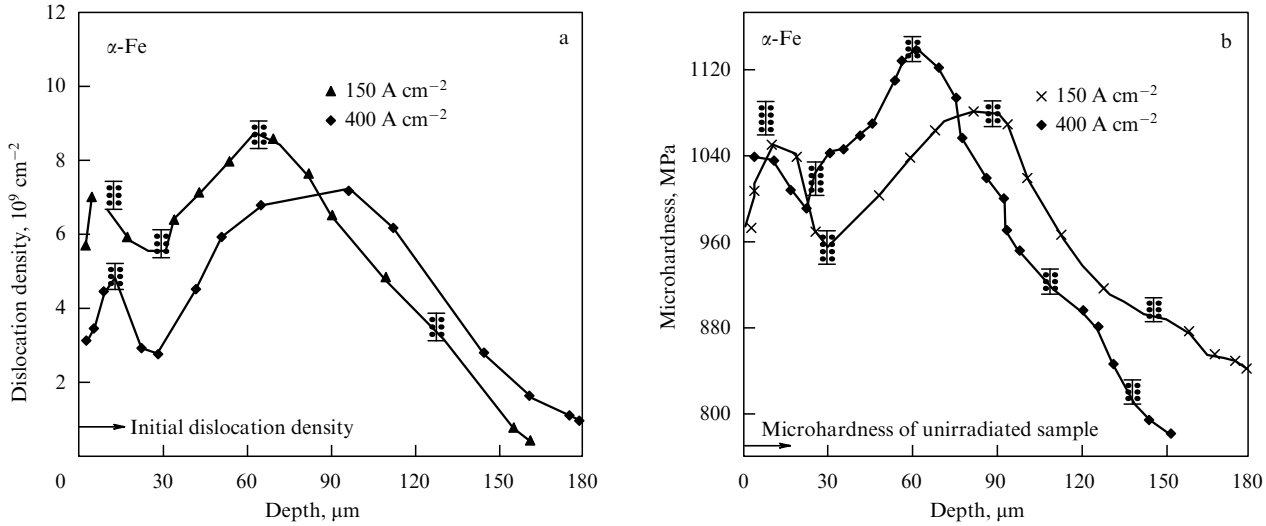

Figure 7. Depth profiles of (a) the average scalar dislocation density and (b) microhardness of the modified layer of α-Fe irradiated with an HIB in different regimes.

evaporation of a fraction of the surface layer. Hence, beginning at a certain threshold value of j, the thickness of the melted layer decreases due to evaporation and ablation, with the result that the liquid–solid boundary, at which the gradient of thermomechanical stresses and the dislocation density are maximum, are localized closer to the surface.

The other (more wide) peak at $j = 400$ A cm^{-2} is formed at a depth of roughly 70 μm and has a value $H \sim 1150$ MPa. At 150 A cm^{-2}, these values are ~ 90 μm and 1080 MPa, respectively. As j and Φ increase, the absolute value of H increases only slightly, and the shift of the peaks closer to the surface in these distributions is related to the specific features of the formation of the wavefront of SW (these features are examined in Section 3.4). The depth of the modified layer with elevated values of the dislocation density and microhardness reaches 200 μm for an irradiation depth of roughly 1 μm (see Fig. 7). The shift of the second peak in H is noticeable, while the shift of the first peak depending on the irradiation regimes is less pronounced. The strain hardening is determined by the dislocation structure.

Valyaev et al. [69, 77] performed a detailed analysis by applying a low-energy beam of positrons (0.2–30 keV with energy changed in small steps) and by the RBS/C method in a layer with a thickness less than 1 μm suffered a remelting and partial evaporation under irradiation. As a result of quenching from the liquid state, the concentration of vacancy clusters and dislocations that emerge in the layer increases considerably, which is indicated by the increase of the S parameter in comparison to the initial value. In the layer where maximum thermomechanical stresses are observed (the boundary between the liquid and solid phases), a high dislocation density (6.5×10^9 cm^{-2}) and a substantial concentration of vacancy clusters ($5 \times 10^{17} - 10^{18}$ cm^{-3}) arise. The RBS data indicate a substantial rise in the concentration of interstitial atoms for the [100] and [001] directions in comparison to the initial oriented crystal with a coarse grain (2–4 mm), with the concentration being highest in the [100] direction. Only slight changes in the concentrations of carbon and chromium in the surface region (up to 7 μm thick) caused by irradiation indicated that no carbide and oxide layers were formed [69]. The fact that there is agreement between the electron-microscopic, RBS, EPA, and SIMS results and the variations of microhardness support the proposed mechanism of dislocation strain hardening of the surface layer of α-Fe. However, the long-range effects can hardly be explained in this way. To establish the nature of such effects, special experiments described in Sections 3.2 and 3.3 were performed.

3.2 Analysis of residual deformation states

Since the formation of strain-hardened layers in metals irradiated with an HIB is determined by a definite spatial distribution of structural changes, certain residual deformation states should correspond to this process. To analyze such states, a new method has been developed [69, 78], which incorporates the nondestructive nucleus recoil method used to obtain the depth distribution of hydrogen [79]. Samples of single-crystal lead of 99.98% purity were irradiated with an HIB (5.5 J cm^{-2} per pulse). For unirradiated samples, the microhardness distribution $H(x)$ remained unaltered with depth (Fig. 8a), whereas for the irradiated samples two peaks were found. Then the samples were saturated with hydrogen. Hydrogen does not chemically react with lead, which explains why lead was chosen as the object of investigation. The degree of saturation of lead with hydrogen determines the hydrogen concentration n_H at a given depth, which was found to be the same for the unirradiated samples ($n_{H0} \sim 5.2$ at. %). After irradiation the distribution $n_H(x)$ becomes highly nonuniform, with four layers becoming clearly visible (Fig. 8b): L1 and L3 are the compression regions, where the hydrogen saturation is low ($n_H < n_{H0}$), and L2 and L4, the regions of tension, which are easily penetrated by hydrogen ($n_H > n_{H0}$). Obviously, this saturation is higher in regions with enhanced vacancy content $n_v(x)$ and low content of interstitial atoms $n_i(x)$ which is characteristic of dilatation regions. For the compression regions the situation is just the opposite. Then, the stress σ at depth x and the degree of deformation ε can be estimated as [69, 78]

$$\varepsilon \sim \sigma \sim \ln \left| \frac{n_H(x)}{n_{H0}} \right| \sim \ln \left| \frac{n_i(x)}{n_{i0}} \right| \sim \ln \left| \frac{n_v(x)}{n_{v0}} \right|, \qquad (3.1)$$

where $n_{i0}(x)$, $n_{v0}(x)$, $n_{H0}(x)$ and $n_i(x)$, $n_v(x)$, $n_H(x)$ are the concentrations of interstitial atoms, vacancies, and hydrogen

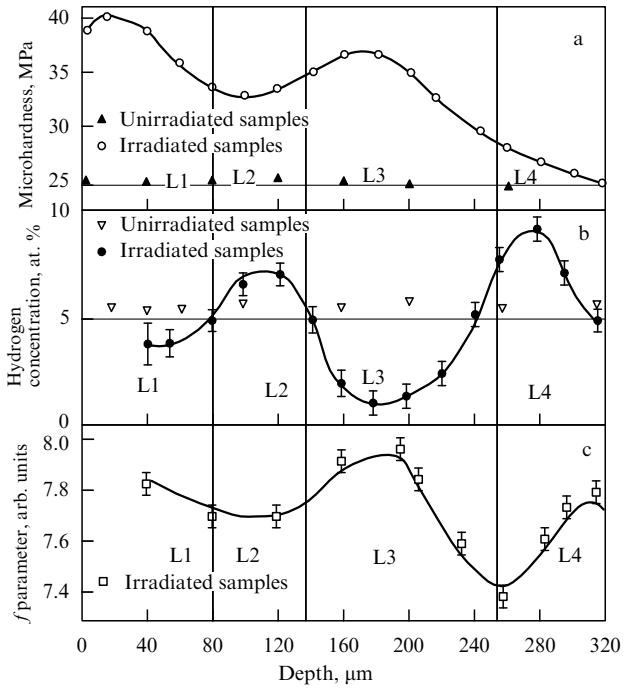

Figure 8. Distributions of microhardness, hydrogen concentration, and the f parameter over the depth of the lead target irradiated using an HIB (0.2 – 0.6 MeV, 100 ns, 5.54 J cm^{-2} per pulse).

atoms before and after irradiation, respectively. The method of diagnosing defects by the curves representing the angular distribution of annihilation photons (ADAP) [80] makes it possible to find the value of the f parameter at different depths:

$$f = \left| \frac{N(0) - N_b}{N(10) - N_b} \right|, \qquad (3.2)$$

where $N(0)$ and $N(10)$ are the counting rates at the peak in the ADAP curves for angles equal to 0 and 10 mrad, and N_b is the background counting rate. Prior to irradiation, this value was the same for all depths (Fig. 8). After irradiation, the shape of the ADAP curves changes, and the corresponding depth dependence of the f parameter becomes complicated due to the high sensitivity of this parameter to the concentrations of dislocations, point defects, and aggregates of defects such as pores and clusters. Clearly, all three types of distribution are linked. Since lead is a low-melting metal, signs of melting were observed in the surface region after irradiation, which made it more difficult to extract reliable information about the values of H, n_H, and the f parameter. Note that for lead, in contrast to other metals, the height of the second peak of microhardness is close to its value in the surface region, and it is localized in the target at larger depths (160 – 200 μm). This is due to the mechanical and thermophysical properties of lead, which determine the characteristic feature of SW propagation in lead. The lower melting and boiling points of lead correspond to higher values of mass being carried away and the rate at which the process takes place for the same fluence as for other metals. These factors cause the recoil impulse transferred to the target to become larger, which creates higher compression of the material and increases the initial SW amplitude.

Four layers of deformation are formed after irradiation (see Fig. 8): L1 (up to 80 μm) is the compression region with an elevated concentration of interstitial atoms and dislocations and corresponds to the first peak of microhardness; L2 (80 – 130 μm) is the region of tension with a higher concentration of vacancies and vacancy-type dislocation loops; L3 (130 – 250 μm) is the compression region with an elevated concentration of interstitial atoms, dislocations, and dislocation pileups (the region of the second microhardness peak); and L4 (> 250 μm) is the region of tension where all transitions die down and the structure of the material approaches the initial structure. This is the reason why lead was used in the experiments. But is it possible to extrapolate the results to other metals, since lead has specific mechanical (low microhardness and high plasticity) and thermophysical properties? The following results are important for all metals, including lead:

(1) The depth distribution of microhardness of the irradiated target has two peaks, which differ somewhat in their quantitative parameters (see Fig. 7). This is an indication that, for the same irradiation regimes, a single mechanism of formation of strain-hardened layers is operative.

(2) EPA analysis shows that the nature of the depth distribution of structure-sensitive defects is the same.

(3) There is correlation between two types of distribution, $H(x)$ and $f(x)$, and between three types for lead [including $n_H(x)$]. This suggests that it is possible to extend the formulated conclusions to all metals.

3.3 Effect of different types of radiation on bulk strain hardening

Irradiation has different effects on the strain hardening of metals depending on the radiation type, particle energy, intensity, and fluence. Hence, by comparing various effects one can expose the main factor determining bulk strain hardening. To this end, the following experiment was conducted [69]. Four groups of samples were manufactured from a single billet of tool steel R6M5 (composition in at. %: 5.3 W, 4 Cr, 1.5 Mo, 1 V, 0.001 C, with Fe the balance). The first group (the reference), was not irradiated. The samples belonging to the second group were implanted with C^+ ions (40 – 60 keV, 40 – 60 μA cm^{-2}) to a dose $\Phi_i = 1.5 \times 10^{18}$ ion cm^{-2}, or $\sim 1.2 \times 10^4$ J cm^{-2}. The third group was irradiated with a pulse of a high-power ruby laser (with a wavelength of 0.694 μm, 80 ns, $\Phi_l = 5$ J cm^{-2} per pulse). Finally, the fourth group was irradiated with an HIB ($\Phi_{HIB} = 5.5$ J cm^{-2} per pulse). The microhardness H was the same (~ 5.1 GPa) at all depths x for the unirradiated samples (Fig. 9). The doses for all types of radiation were selected in such a way that after irradiation the value H_1 in the surface region was approximately the same. After laser irradiation and HIB irradiation, the recorded values were $H_1 \sim 8.5$ GPa at $x_1 \sim 1-2$ μm in the first case and $H_1 \sim 10.5$ GPa at $x_1 \sim 2-3$ μm in the second. After ion implantation the value of H_1 was about 8.7 GPa at $x_1 < 1$ μm (the error in determining H for all the groups did not exceed 5%).

A distinct difference in the distributions $H(x)$ was observed in all four cases. For unirradiated samples, the distribution was uniform. For implanted samples, H was found to rapidly decrease and to equal the initial value at $x > 3$ μm. After laser irradiation, a second microhardness peak was observed, with $H_2 = H_z \sim 7.5$ GPa for $x_2 = z \sim (35-45)$ μm and the width of the strain-hardened region being $\Delta x = 45-35 = 10$ μm. A similar pattern was observed

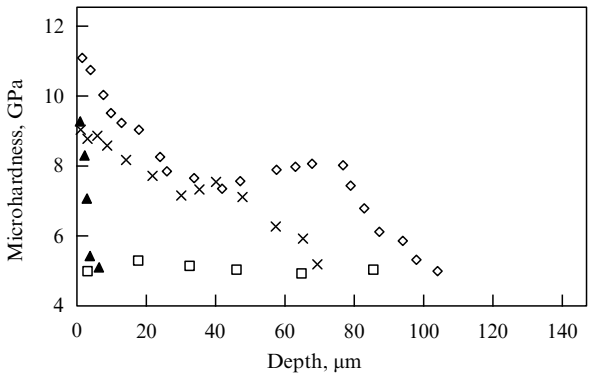

Figure 9. Depth distributions of microhardness in the R6M5 steel after irradiation with different types of radiation: □, the initial sample; ▲, implantation with C^+ ions; ×, irradiation with a laser; and ◇, irradiation with an HIB.

after HIB irradiation, but the second peak was higher, $H_z \sim 8.1$ GPa, formed at larger depths $z \sim 60-80$ μm, and more extended ($\Delta x \sim 20$ μm).

The mechanism of strain hardening of steel after implantation with carbon ions is related primarily to the formation of carbide phases at the surface [43, 81]. The depth of the modified layer depends on the projected range of ions at the given energies (< 0.2 μm). In the case of laser and ion pulsed irradiation, strain hardening at large depths is determined by the effect of SW, which will be described in Section 3.4. The very fact that after laser irradiation the second peak is closer to the surface is related to the steeper and narrower initial profile of the deposited energy [4]; the penetration depth of the radiation is in this case roughly 0.1 μm, which is ten times smaller than for HIB irradiation (see Fig. 5). Note that after irradiation of α-Fe with an LHEB, in which case only a small-amplitude (< 0.1 GPa) elastic wave was generated, no strain hardening at large depths was observed [62, 63]. Thus, the given experiment corroborates the decisive role that SW plays in bulk strain hardening.

Let us estimate the amounts of energy contributed by these effects to strain hardening. Close values of the microhardness increments were obtained for equal fluences of the laser and HIB irradiation. The energy contribution to strain hardening in the case of ion implantation was at least three orders of magnitude smaller: $\Phi_i/\Phi_l \approx \Phi_i/\Phi_{HIB} \sim 10^3$, and the effect was achieved only in the surface layer. This thin layer deteriorates very rapidly under mechanical stresses at the surface of steel products, such as boring, milling and cutting tools. A promising approach to increasing wear resistance is to use high-power laser and ion beams, which boost bulk strain hardening. In this case the L2 layer of the material, whose microhardness lies between the two peaks and whose characteristic feature is the presence of residual tensile strain (see Fig. 8), acts as a buffer, which is especially effective in increasing the resistance of the material to impact. This feature can be used in developing armor, protective screens, etc. It is more advisable to use HIBs than lasers, since the overall effect of surface and bulk strain hardening is larger for equal fluences and the efficiency of HIB accelerators is roughly ten times the efficiency of lasers.

A report on detailed studies of how HIB irradiation regimes affect the characteristics of bulk strain hardening of R6M5 steel can be found in Ref. [69]. The following empirical formulas were obtained for the dependence of the height of the second microhardness peak H_z (GPa) and the depth z (μm) at which this peak is formed, on the current density j:

$$H_z = 685\left(\frac{j}{100}\right)^{0.43}, \tag{3.3}$$

$$z = \frac{150}{(j/100)^{0.95}}. \tag{3.4}$$

These results agree with the data on α-Fe (see Fig. 7): as j and the fluence get larger, H_z increases and there is a shift of z toward the irradiated surface. Note that the distribution $H(x)$ correlates with the corresponding depth distribution of resistance to wear of steel samples in friction against an abrasive material. A similar correlation was also observed for copper [10] and beryllium [69].

3.4 Kinetic model of strain hardening

The experimental and theoretical substantiation of the model of bulk strain hardening comes from the following results:

(1) The effect has been discovered for many materials that differ in structure and mechanical and thermophysical properties, such as Al, Cu, W, α-Fe, Be, Pb, and also R6M5 steel.

(2) The effect is nonlinear and manifests itself at irradiation fluences and intensities exceeding certain critical (threshold) values. It is stable and clearly visible, i.e., the microhardness distribution has two peaks of almost the same height at entirely different depths, with two corresponding depth distributions of resistance to wear.

(3) For different irradiation regimes, there is a strong correlation between the average scalar dislocation density and microhardness, both in the surface layer and in the bulk.

(4) Despite the different spatial distributions of microhardness, the character of distribution of residual deformation states is the same in all the metals.

(5) The long-range effect manifests itself only after highly intense pulsed irradiation, and the main contribution is provided by the shock wave, while the elastic wave does not produce such an effect.

Let us estimate the thickness of the heated layer in the course of the irradiation pulse ($\tau_p \sim 10^{-7}$ s): $x_h \sim (\chi\tau_p)^{0.5}$, where χ is the thermal diffusivity ($\chi = 0.8-2$ m^2 s^{-1} for most metals). The value $x_h \sim 1-2$ μm (which corresponds to the projected ranges of medium-energy protons), with the result that one can ignore the amount of heat removed into the target in the course of the pulse and losses to radiation. This practically instantaneous heating of the metal in the surface region causes (a) thermal stresses in the solid phase (thermal shock), and (b) melting and ejection of matter from the irradiated surface. The recoil impulse generated causes additional compression. The two processes create a pressure P in the target equal to

$$P = P_1 + P_2 = \Gamma_1 W_1 + \Gamma_2 W_2, \tag{3.5}$$

$$W = W_1 + W_2, \tag{3.6}$$

where P_1 and P_2 are the pressures generated by the first and second processes, W_1 and W_2 are the components of the density of the total deposited energy (dose) W that causes these pressures, and Γ_1 and Γ_2 are the Grüneisen constants for the solid phase and plasma in ablation. Experiments have

revealed that when high-power pulsed beams irradiate metals, the pressure P_2 becomes important at intensities that are several orders of magnitude higher than those reached in our experiments [4, 82]. Then, the initial pressure profile $P(x, t = 0)$ is determined by the distribution of the absorbed dose $W(x)$:

$$P(x, t = 0) = P_1 = \alpha_1 \Gamma_1 W(x) . \tag{3.7}$$

Direct measurements of the amplitude of the SW compression pulse yielded the estimate $\alpha_1 = 0.1$, i.e., only roughly 10% of the beam's energy goes into the generation of a shock wave [66]. But is the generated wave indeed a shock wave? The criterion for the generation of a shock wave produced by laser irradiation [83] is valid for all thermal effects of concentrated pulsed energy fluxes on absorbers and has the form

$$\frac{Q}{n\tau_p^2} > \frac{C_L^4 \rho_0}{\mu_\lambda} , \tag{3.8}$$

where Q is the total absorbed energy of the pulse of length τ_p, n is the number of peaks, C_L is the speed of longitudinal sound, ρ_0 is the density, and μ_λ is the absorptivity of the radiation by the material prior to irradiation. When an HIB is used, $Q = IS\tau_p$, $\mu_\lambda = R_0^{-1}$, and $n = 1$, with criterion (3.8) becoming

$$\frac{IS}{\tau_p} > C_L^4 \rho_0 R_0 , \tag{3.9}$$

where I is the intensity of irradiation, S is the area being irradiated, and R_0 is the ion range in the material. In the commonly used irradiation regimes $I \sim 10^{12}$ W m^{-2}, $\tau_p \sim 10^{-7}$ s, and $S \sim 10^{-4}$ m^2 for iron ($C_L = 5 \times 10^3$ m s^{-1}, $\rho_0 = 7.9 \times 10^3$ kg m^{-3}, $R_0 \sim 1$ μm), so that we obtain $IS/\tau_p \sim 10^{15}$ kg m^2 s^{-4} and $C_L^4 \rho_0 R_0 \sim 10^{12}$ kg m^2 s^{-4}. Thus, the criterion for SW generation is met and the initial pressure in such a wave is several GPa, i.e., the wave is weak (< 10 GPa) [69, 77].

What is important in the proposed mechanism of bulk strain hardening is that the parameters of the shock wave generated by an HIB are close to those of a laser shock wave (LSW). It has been established through experiments [41, 42, 83–87] that the LSW characteristics differ markedly from those of waves generated by an explosion or a high-speed collision: the duration of the compression phase of such a shock wave is about 1000 times smaller and the pressure range is broader (from acoustic pressures to 10^{14} Pa). Hence, at the atomic level, the action of an LSW on solids differs dramatically from that of a mechanical stress wave and is largely determined not by the amplitude of the pressure but by the pressure's spatial gradient. This is the cause of a number of new effects recorded by the changes in the mechanical and electrical properties of metals and semiconductors generated by LSW. According to Yanushkevich [87], a laser shock wave is a flow of nonequilibrium phonons. When these phonons interact with the irregularities in the lattice, the scattering center acquires momentum and forms a defect. Here momentum transfer from the excited atoms to the unexcited ones manifests itself as an individual effect rather than a cooperative one. The LSW deforms the lattice along a single direction, thus generating lateral displacements of the atoms. Hence, the energy threshold for defect formation in an LSW is approximately 100 times lower than that corresponding to ordinary loading for the same injected energy density. As a result, the role of impurities, defects, and fluctuations grows significantly. This conclusion is corroborated by experiments, where it was discovered that LSW acts selectively on impurities such as boron and iron present as dopants in germanium and silicon [86].

At the macroscopic level, the propagation of an SW into the unirradiated region compresses the metal, which facilitates grain refinement. This increases the microhardness of the metal with pressure according to the law $H \sim P^{0.5}$ [73, 88]. The pressure of the wave decreases with increasing depth, which first causes a reduction in H (see Figs 7–9). However, the wavefront of the SW becomes steeper (we will corroborate this by calculations). The initial value of the pressure gradient is determined by the initial distribution $P(x, t = 0)$ [see (3.7)]. It is then calculated according to the changing pressure profile in the wave proper. The pressure gradient increases, reaching its maximum in the region where the wavefront of the SW is formed. The most intense generation of intrinsic and impurity defects corresponding to the maximum of spatial distortions occurs in this region. The typical type of defect in metals is a Frenkel pair: an interstitial atom and a vacancy. Interstitial atoms are much more mobile than vacancies, whereby their flow to sinks (dislocations) fixes the vacancies, reducing the mobility of the latter. This results in an increase in the yield stress and microhardness. The width of the wavefront of the SW at pressures of about 10 GPa amounts to thousands and hundred thousands of interatomic distances [72, 89]. Thus, the appearance of a second microhardness peak at large depths agrees fully with such an interpretation and corresponds to a real process.

Both the atoms of the matrix and the defects (scattering centers) acquire momentum from the SW. But the latter, due to the difference between the mass of defects and that of the atoms of the main element and due to local microdistortions, acquire additional momentum $\Delta\Pi$ [87]:

$$\Delta\Pi \sim \left(\frac{\Delta A}{A}\right)^2 + \left(\frac{\Delta\sigma}{\sigma}\right)^2 , \tag{3.10}$$

where ΔA and $\Delta\sigma$ are the local changes in the atomic weight and the elastic modulus introduced by a scattering center (A and σ refer to the matrix). Since the diameter of the irradiation spot exceeds the ion range substantially, the shock wave is a plane wave, and to find its profile one must use one-dimensional differential equations for the laws of mass and momentum conservation and the equation of state. These equations were solved by the net method using the algorithm developed in Ref. [90]. The region of formation of the wavefront of the SW can be found from the value of the depth $x = z$ at which the derivative $(\partial P/\partial x)_{x=z}$ is at its maximum. Figure 10 depicts the results of calculating the distributions of the pressure gradient determined by the pressure profile in the wave proper.

The kinetic equations in this region allow for the generation of Frenkel pairs, their recombination, and the flowing of interstitial atoms to sinks such as dislocations [69, 90]. Assuming that the increase in microhardness H_z is a linear function of the number of defects flowing to dislocations, we find that

$$H_z = K_1 K_2 \sqrt{j} , \tag{3.11}$$

where the coefficient K_1 is determined by the properties and structure of the material, the coefficient K_2 depends on the

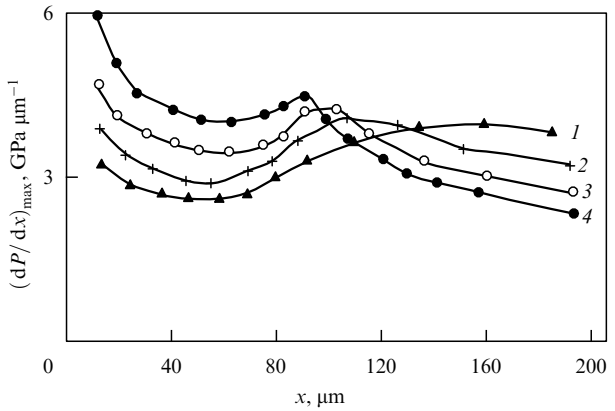

Figure 10. Depth distributions of the SW pressure gradient in an iron target irradiated with an HIB at different fluences: *1*, 3.3; *2*, 3.5; *3*, 4.4; *4*, 5.5 J cm^{-2} per pulse.

SW profile, and j is the current density in the beam at the target. Explicit expressions for K_1 and K_2 can be found in Ref. [69]. The dependence $H_z \sim j^{0.5}$ is in good agreement with the experimental dependence $H_z \sim j^{0.43}$ [see (3.3)]. The position of H_z is determined by the region of localization of the maximum value of the pressure gradient in the SW (see Fig. 10). As the current density grows and hence the irradiation fluence increases, the absorbed dose and the corresponding initial pressure of SW increase. According to the general theory of propagation of shock waves in solids [91], this leads to a faster formation of the wavefront of the shock wave at smaller depths. Indeed, all depth dependences of $\partial P/\partial x$ have peaks localized at different depths $x = z$, with larger values of j corresponding to larger values of $(\partial P/\partial x)_{max}$ and smaller values of z, which is also in good agreement with the experimental data [see Fig. 10 and Eqns (3.3) and (3.4)].

The main conclusions that can be drawn from the material of this section are as follows:

(1) For a broad range of HIB irradiation intensities, there exists a correlation between the bimodal distributions of the dislocation density and the microhardness with respect to the depth of the modified layer, a correlation that corroborates the crucial role of the dislocation structure in bulk strain hardening.

(2) The modified layer has four regions with different behaviors of the residual deformation states corresponding to the microhardness distribution.

(3) Bulk strain hardening occurs only when the sample is subjected to high-power pulsed radiation capable of generating a shock wave.

(4) High-power ion beams contribute the greatest amount of energy to this effect and form the most extended strain-hardened layers, which ensure a substantial increase in the resistance to wear in comparison to other types of radiation.

(5) The proposed kinetic model of transformations in the field of a shock wave is in good agreement with the experimental data. The laws that follow from the model suggest the possibility of predicting or purposefully altering the properties of materials by selecting a specific regime of HIB irradiation. This effect is the basis of a new method of processing metals with the aim of increasing their resistance to wear and durability [92].

The results presented here are in good agreement with the most recent investigations carried at the Sandia National Laboratory (New Mexico, USA) on a PHEPP-I proton accelerator (0.8 MeV, 60 ns, 25 kA) [93]. After irradiation of the structural steel AISI304L (19% Cr, 9% Ni, 0.03% C) with a fluence of 1.6 J cm^{-2} per pulse, an increase in microhardness was observed at large depths (up to 140 μm), although the irradiation depth was roughly 6 μm. Microscopic observations revealed a distinct bimodal distribution of the dislocation density in an irradiated titanium target at two depths, ~30 μm and ~100 μm (prior to irradiation the surface of the target was alloyed with a thin film of platinum, ~2 μm). Renk et al. [93] state the presence of long-range effects and agree that their results correspond to those of the present authors.

Such effects also clearly manifest themselves in the way a shock wave generated by a laser pulse (0.6–2.5 ns, 120–2050 GW cm^{-2}) acts on iron: there is a substantial increase in the quantity of twins at depths from 50 to 400 μm [94].

4. Melting and mixing of two-layer metallic systems irradiated with a low-energy high-current electron beam

When the surface of one material is covered by a thin film of another material, subjecting this system to a high temperature for a short time may lead to mixing of the components and to redistribution of the elements of the film and substrate, accompanied by formation of various compounds in addition to annealing processes. Recently, HIB and HEB have been used for rapid liquid-phase mixing of thin surface layers. The study of this phenomenon is fundamental if one wants to build nonequilibrium phase diagrams, since such irradiation can produce nonequilibrium compounds and metastable phases whose existence in equilibrium phase diagrams is forbidden. A series of studies of systems characterized by different miscibilities, such as Ag–Fe, Cu–Fe, Al–Fe, Au–Cu, Au–Cu–Mo, Mo–Zn, Fe–Pb, Fe–Si and others, suggest that this is the case for systems not only with a high solubility but also with limited solubility or complete immiscibility [11, 55, 56, 77, 95–99].

Of special interest is the possibility of mixing materials with very different thermophysical and thermodynamic properties, which is difficult to do by traditional methods. It is important to study the modifications at the surface of iron, which serves as the base element for steels and alloys with new structures, doped with various elements. For instance, the high-melting metals Ta and Mo improve mechanical, thermophysical, and corrosion-resistance properties of iron. The melting points T_m of Fe, Ta, and Mo are 1537, 2997, and 2617 °C, respectively, while the boiling point of Fe, equal to 2872 °C, lies between T_m for Mo and Ta, which makes the introduction of Mo and Ta into the matrix much more difficult. The equilibrium diagrams of the Ta–Fe and Mo–Fe systems are characterized by unlimited mutual solubility of the components in the liquid phase and limited solid solubility; the Fe–Ta system contains two compounds, FeTa and Fe_2Ta with a broad homogeneity range. When the concentration of Ta is 42% ($T = 1550$ °C), an $Fe_2Ta + FeTa$ eutectic crystallizes, and when the concentration of Ta is 64% ($T = 1680$ °C), the FeTa + Ta eutectic is formed. The solubility of Ta in γ-Fe amounts to less than 3% and in α-Fe, no more than a few tenths of an atomic percent [100]. The motivation of research stemmed from the possibility of using LHEBs for mixing such systems, analyzing the element and phase composites that are formed in the process, and investigating the effect of these composites on the modified properties [69, 101].

In simulating the thermal regimes for pure α-Fe [63] and the Ta – Fe and Mo – Fe systems, the dynamics of the temperature field was analyzed numerically by solving a one-dimensional heat transfer equation with variable values of the heat capacity and the thermal diffusivity in the presence of a heat source specified by the irradiation regime [102]. Phase transitions including melting and solidification processes were taken into account [103]. Figure 11a depicts the curves that represent the time dependence of the position of the melt – solid phase boundary for a Ta – Fe system consisting of a thin (100 nm) Ta film on an α-Fe substrate (100 μm) for different fluences Φ. As Φ increases from 2.3 to 5.2 J cm^{-2} per pulse, the thickness of the melted layer of iron and the time of its existence increase within the ranges 2.7 – 7.8 μm and 2 – 10 μs. But when α-iron was irradiated with the same fluences, these two quantities were found to vary within the ranges 0.7 – 2.5 μm and 0.5 – 3 μs, respectively [63]. The solid curves (Fig. 11a) correspond to sections where $T = T_m$ and the metal is in a metastable two-phase state (slush state) that appears only under pulsed heating, when not all of the heat required for complete fusion is introduced into the system [104]. Figure 11b depicts the effect of Φ during the time when the Ta film exists in the liquid state. When $\Phi = 2.5$ J cm^{-2} per pulse, the film has not yet melted and the thickness of the molten layer of Fe is 2.7 μm (curve *1*). When $\Phi = 3.3$ J cm^{-2} per pulse, the components melt simultaneously within a time of 0.4 μs. When $\Phi = 5.2$ J cm^{-2} per pulse, this time grows to 1 μs. As Φ increases, the maximum cooling rate of the melt at the surface decreases from 10^9 to 10^8 K s^{-1}, and the velocity of the wavefront drops from 2 to 1 m s^{-1}. When α-Fe is irradiated, the values of these characteristics amount to $10^{10} - 10^9$ K s^{-1} and 2 – 5 m s^{-1}, respectively. Thus, the presence of a high-melting film substantially (by a factor of four) increases the thickness and lifetime of the molten layer of iron, which lowers the rate of quenching from the melt and slows down the solidification process. Nevertheless, the values of these characteristics are sufficient to ensure effective trapping of impurities by the melt – solid interface and to largely prevent segregation of dissolved impurities in the course of solidification.

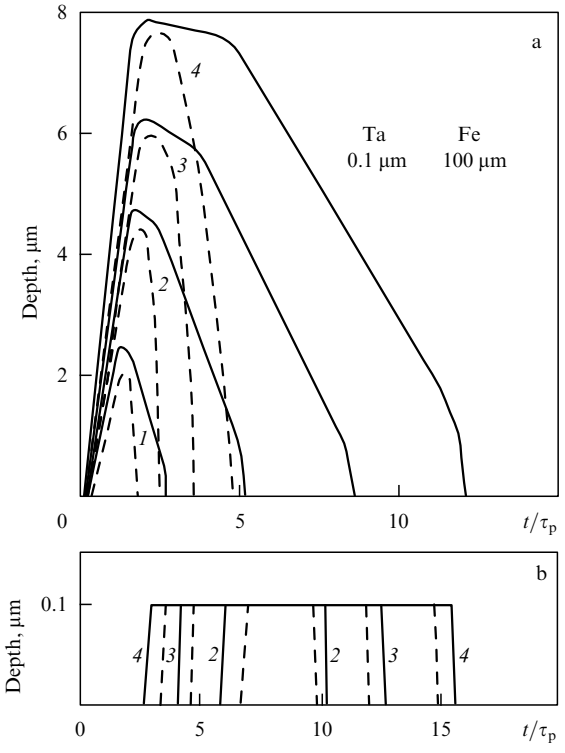

Figure 11. (a) Time dependence of the position of the interphase interface in the Ta – Fe system subjected to a single LHEB pulse (6 – 20 keV, 0.8 μm) for different fluences: *1*, 2.3; *2*, 3.3; *3*, 4.2; and *4*, 5.2 J cm^{-2} per pulse. (b) The effect of fluence on the kinetics of melting of the Ta film (100 nm thick). Solid curves represent the slush state of the system, consisting of the solid and liquid phases, and the dashed curves represent the liquid phase.

Figure 12 depicts the energy spectra of RBS for the Ta – Fe system before and after LHEB irradiation. The decrease in the height of the Ta peak and the smearing and shift of the right edge of the spectrum to the left suggest that irradiation leads to a mixing of the components at all values of Φ, including $\Phi = 2.5$ J cm^{-2} per pulse, when according to calculations (Fig. 11b) the Ta film does not melt. When Φ is large, the spectra acquire horizontal sections, which corroborates the formation of layers with a thickness of up to 100 nm with a constant concentration of Ta. The decrease in the height of the Ta peak as Φ decreases suggests that the mixing is accompanied by a loss of the mass of Ta, most probably due to Ta spitting by the overheated vapors of the substrate. The results of Auger electron spectroscopy (AES) show that the initial film contains, in addition to Ta (about 60 at. %), a sizable amount of carbon and oxygen. The maximum concentration of oxygen is observed at the film – substrate boundary, which corroborates the formation of a tantalum oxide layer. After irradiation, a redistribution of the elements of the film and substrate occurs and they become thoroughly mixed, a fact agreeing with the RBS data. There is also an increase in the concentration of oxygen in the surface layer with a thickness of to 50 nm accompanied by the formation of

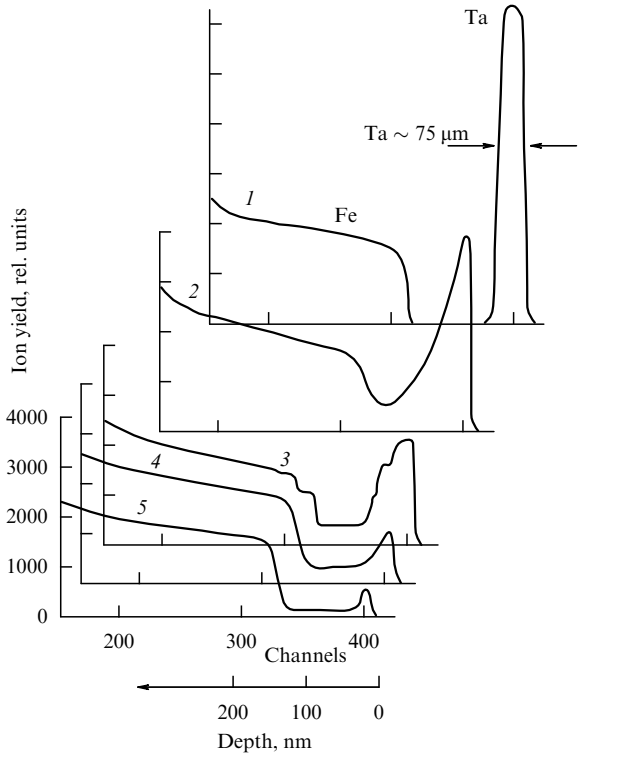

Figure 12. Energy spectra of RBS of $^4He^{++}$ ions (1.8 MeV) for the Ta/Fe system (*1*) before and (*2* – *5*) after LHEB irradiation: *2*, 2.3; *3*, 3.3; *4*, 4.2; and *5*, 5.2 J cm^{-2} per pulse.

an oxide layer whose thickness decreases with increasing Φ, while the depth of the mixed layer increases to 250 nm. An analysis of the Ta profiles based on the RBS and AES spectra shows that with increasing Φ the concentration of Ta strongly decreases both at the surface and in the bulk and that at high fluences, e.g., $\Phi = 5.5$ J cm^{-2} per pulse, the major fraction of the Ta film is carried away due to ablation.

The effective diffusivity of Ta in the liquid phase calculated by Fick's equation amounts to $(3-8)\times 10^{-5}$ cm^2 s^{-1}. These values are characteristic of diffusion in such a phase [97, 105, 106]. We believe that the following reasons explain the mixing of Ta and Fe at $\Phi = 2.5$ J cm^{-2} per pulse, when according to the results of calculations of thermal fields the Ta does not melt. The calculations did not allow for the existence in the Ta–Fe system of the δ-Fe + Fe_2Ta eutectic, which is formed at 7.9 at. % of Ta and melts at $T = 1440$ °C [100], and for the presence in the initial layer of Ta oxide, whose thermal conductivity is much lower than that of Ta. These two factors can lower the melting threshold to $\Phi = 2.5$ J cm^{-2} per pulse, with the melting beginning not at the surface but at the film–substrate interface.

Figure 13 shows the morphology of the sample's surface before and after irradiation [101, 107]. The initial coating is inhomogeneous (Fig. 13a). After irradiation this inhomogeneity increases (Fig. 13b). The larger fraction of surface has a structure characteristic of the eutectic. Three sections that differ in contrast can be specified here, T_1, T_2, and T_3, with T_1 and T_2 taking up 30 and 50% of all the area, respectively. Microprobe analysis has shown that the dark sections T_1 mainly contain iron, the light sections T_3 mainly contain Ta, and the gray sections T_2 contain a mixture of these elements in comparable concentrations. Hence, the mixing process effectively occurs only in the T_2 sections, which amounts to 50% of the irradiated area. We believe that the inhomogeneity of mixing is due to the nonuniformity of the coating itself, both along the surface and into the film (Fig. 13a), and also to the ejection of some of the coating in the flashing (burst boiling) of the substrate (at $\Phi = 5.5$ J cm^{-2} per pulse the temperature at the surface reaches 4000 °C).

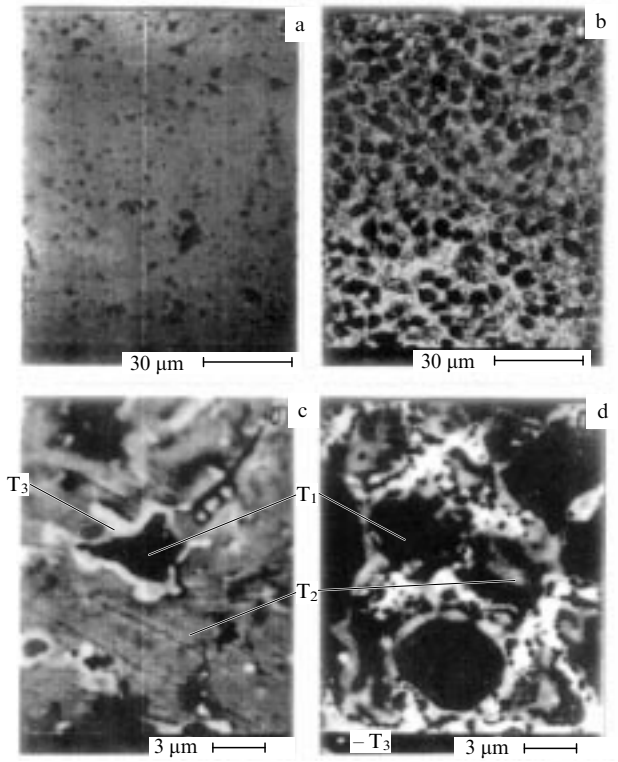

Figure 13. Morphology of the surface of Ta/Fe samples: (a) prior to irradiation in the initial state; (b) after LHEB irradiation (3.5 J cm^{-2} per pulse); (c) initial state (large magnification); (d) after LHEB irradiation (3.5 J cm^{-2} per pulse).

The most interesting are the T_2 sections, which contain 0.3-μm spherical particles of undissolved Ta and 30-nm particles of the intermetallic compound Fe_2Ta (Fig. 14a and 14b). The diffuse ring in the electron-diffraction pattern (Fig. 14b) suggests that an amorphous Fe–Ta phase has been formed. Since at the surface the concentration of Ta is high, we may assume that a substitutional solid solution Fe(Ta) has also been formed. According to the intensities of the reflections of Fe (Fig. 14b), the volume fraction of Fe(Ta) is much smaller than the volume fractions of Ta and Fe_2Ta, with Fe_2Ta being the main phase [100]. Observations show that at a depth of 0.3 μm (Fig. 15d) there are grains of the solid solution with an enhanced (8×10^9 cm^{-2}) dislocation density (in the initial α-Fe this density is on the order of 10^8 cm^{-2}) and 50-nm particles of Fe_2Ta. No traces of an amorphous phase were found. At depths larger than 0.5 μm, randomly distributed grains of α-Fe with an enhanced dislocation density were revealed. Such densities are created by thermoelastic stresses generated by the rapid solidification of the molten layer [108, 109]. Additional contributions are provided by stresses caused by the transformation-induced hardening in the process of the $\gamma \rightarrow \alpha$ transformation. This fact is corroborated by the results of conversion-electron Mössbauer spectroscopy [69, 101].

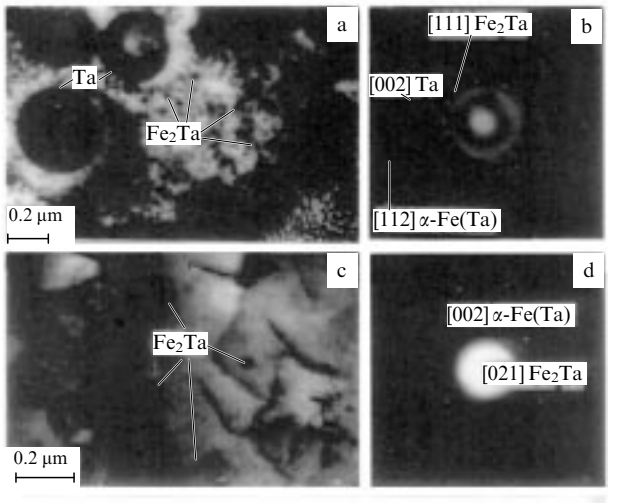

Figure 14. Electron-microscopic study (TEM) of the Ta/Fe system irradiated with an LHEB (3.5 J cm^{-2} per pulse, 0.8 μm): (a, c) micrographs taken at a depth of 300 nm; and (b, d) microdiffraction patterns.

Figure 15 schematically depicts the structure of the mixed surface layer. The diversity of structures and their layered nature are due to the nonuniform depth distribution of Ta and the difference in the rates of cooling at the surface and in the deeper layers of the melt. The microhardness, measured by a diamond nanoindenter, was found to be different in the regions T_1, T_2, and T_3. Maximum hardening was achieved in T_2, which also had the greatest resistance to brittle fracture.

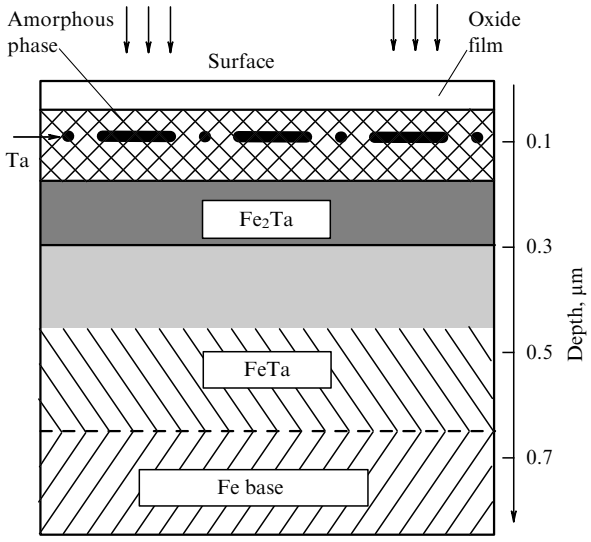

Figure 15. Structure of the surface layer of the Ta/Fe system after LHEB irradiation (schematic).

The experiments determined the optimum regime of irradiation, $\Phi = 3.3$ J cm^{-2} per pulse, which corresponds to maximum hardening. Figure 16 depicts the curves representing the dependence of H on the load for the regions T_1 and T_2; these curves were used to determine the depth of the hardened layer, $\sim 12-15$ μm, which is much larger than the thickness of the mixed layer ($0.1-0.5$ μm). The average increase in microhardness with respect to the initial value reached 0.7 GPa for T_1 and 2.7 GPA for T_2. Processing in the optimum regime also improved the corrosion resistance of the system. A test in saturated water vapor for 36 h showed that the loss of matter for irradiated samples was half that for unirradiated samples. In longer tests (240 h) this difference was found to increase by a factor of ten. Note that similar results have been obtained for the Mo – Fe system [101] and the V – Fe system. Hence, an increase in the mechanical strength and corrosion resistance of steels and iron-based alloys can be achieved by doping the steels and alloys with high-melting elements such as Ta, Mo, and V combined with

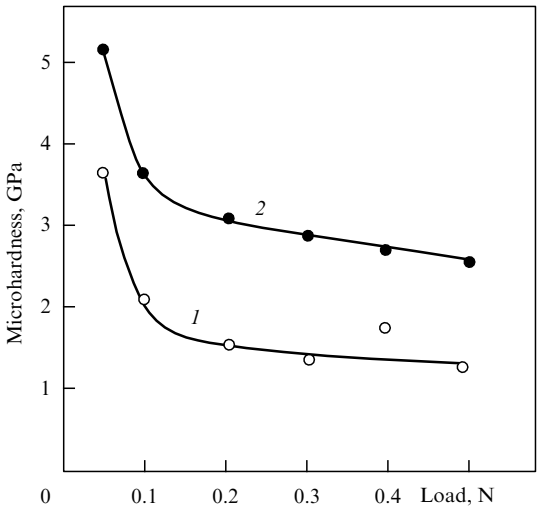

Figure 16. Dependence of microhardness on the load on a nanoindenter for the regions T_1 (curve *1*) and T_2 (curve *2*).

LHEB irradiation of the surface rather then the entire bulk. Thus, there emerges the possibility of realizing a new resource-saving technology.

5. Mass transport due to a high-power pulsed beams of charged particles

One of the possible channels of dissipation of HEB and HIB energy is the intensive transport of atoms in matter. The mechanisms of such transport differ and depend on the thickness of the irradiated target. It is important to study these mechanisms if we want to establish the nature of atom migration in condensed media. While mass transport in the surface layers is determined primarily by diffusion processes due to temperature and pressure gradients, at large depths the main contribution is provided by the shock wave. Here we examine the two corresponding models.

5.1 Mass transport in surface layers

When a system of thin films of Al (0.8 μm) on a Nb substrate and Ag (0.1 μm) on a Cu substrate were irradiated with an HIB (0.5 MeV, 200 ns, 120 – 170 A cm^{-2}), it was found that the film atoms penetrate the substrates to depths that exceed the initial film thicknesses severalfold [110 – 112]. It was also found that the penetration gets deeper as the number of irradiation pulses increases. If we take the duration of the diffusion processes to be the time that the liquid phases exists on the sample's surface, estimates of the effective diffusion coefficients yield $D \sim 10^{-2}-10^{-4}$ cm^2 s^{-1} [112], which exceeds the value for liquid metals by several orders of magnitude. In view of the low beam fluence ($< 10^{14}$ ion cm^{-2}), this intensive mass transport cannot be explained by the presence of ballistic processes. A report of such an effect can be found in Ref. [113], while a similar effect caused by laser and electron irradiation was reported in Refs [114, 115].

Irradiation by HIB generates powerful nonequilibrium temperature and pressure fields in the sample, whose calculated gradients are as high as 10^9 K m^{-1} and 10^{14} Pa m^{-1}, respectively [111]. In addition to the flux j_C caused by the concentration gradient, the two fluxes that are usually ignored but can become substantial under these conditions are the thermal (j_T) and pressure (j_P) diffusion fluxes [116]. Estimates show that the j_C-to-j_T-to-j_P ratio is usually $1:1:10^{-2}$. Therefore, Krivobokov et al. [111] conducted a detailed study of diffusion in the presence of a temperature gradient, to which end the thermal diffusion equation for the concentration C of the diffusant,

$$\frac{\partial C}{\partial t} = \nabla\left[D\left(\nabla C + \frac{K_T \nabla T}{T}\right)\right] \qquad (5.1)$$

was solved together with the Stefan problem. Calculations were made up to the moment when the sample became completely solid. If the impurity present in the melt has different solubility limits in the solid and liquid phases, it segregates as the solidification front travels [68, 108, 116]. The resulting profile of the impurity concentration is determined by the segregation coefficient (which is the ratio of the solubility limits) and the relationship between the melt stirring intensity (e.g., as a result of diffusion) and the velocity with which the solidification front travels. An analysis of the kinetics of this process in the event of HEB (and HIB) irradiation has shown that the segregation effect can somewhat change the shape of the concentration profile

of the impurity, but this effect does not explain the penetration of the impurity into the bulk, at least when the irradiation is a single act [111].

Another possible factor of enhancement of migration of the atoms is the mixing of matter in the molten layer in a hydrodynamic regime. The reason for this lies in the fine structure of the power of energy release along the surface of the sample, which emerges as a result of either filamentation of the beam (the effect was noted in Refs [117, 118]) or the preferential flow of current along the roughness peaks of the surface. In both cases the size of the energy-release inhomogeneities d_j amounts to several microns. The distribution of the current density along the sample's surface (the y axis) was specified by the function

$$j(y,t) = \bar{j}(t)\left(1 + \cos\frac{2\pi y}{d_j}\right). \tag{5.2}$$

Numerical solution of the system of equations for a continuous medium by Euler's method in the case of an iron target being irradiated by a high-current electron beam (0.9 MeV, 70 ns, 10 kA cm^{-2}) and partial evaporation of the target made it possible to monitor the coordinates of the moving surface of the condensed phase. Zhukov [119] used the equations of state of the target's material. Point markers were introduced into the surface layer of the sample. What was monitored was the displacements of the markers 'along' the depth x, which were calculated in terms of mass units:

$$\Delta x_{\rm m}(t) = \frac{1}{\rho_0}\int_{x_{\rm s}(y_{\rm m},t)}^{x_{\rm m}(t)} \rho(x, y_{\rm m}, t)\,{\rm d}x - x_{\rm m}(0)\,, \tag{5.3}$$

where $x_{\rm m}$ and $y_{\rm m}$ are marker coordinates, $x_{\rm s}$ is the coordinate of the surface, ρ is the density, and ρ_0 is the initial density. It was found that at $j = 10^4$ A cm^{-2} a pressure as high as 10^9 Pa developed in the sample. The velocity of mass transport along the x axis reached $10^2 - 10^3$ m s^{-1}, and along the y axis, 0.1 – 1 m s^{-1}. In the surface layers, $\Delta x_{\rm m}$ is proportional to the depth of occurrence of the markers, $x_{\rm m}$, and the local gradient ${\rm d}j/{\rm d}y \sim d_j^{-1}$. By the time the irradiation pulse has terminated (200 ns), the displacements $\Delta x_{\rm m}$ amount to several tenths of a micron. An analysis of the velocity field in the calculation region $0 \leqslant x < 1$ mm, $0 \leqslant y < d_j/2$ indicated that there was a finite value of angular momentum. It is natural to assume, therefore, that the given vortex motion and the decay of the pressure waves during the time in which there is a liquid phase on the sample's surface (several microseconds) can lead to substantial mixing of the surface layers. Hence, among the mechanisms of intensifying the migration of atoms when high-power beams of particles irradiate a solid, diffusion and thermal diffusion in the molten layer and the mixing of this layer in the hydrodynamic regime play an important role. The segregation of the components of melt in the event of the melt's directional solidification has only a small effect on the shape of the impurity concentration profile.

5.2 Mass transport in an SW field

Olemskoĭ et al. [120] employed a different approach to determine the pressure gradient in the shock wave and used the spatial pressure distribution [121]

$$P = \frac{P_1 + P_2}{2} + \frac{(P_2 - P_1)\tanh(x/\delta)}{2}\,, \tag{5.4}$$

which was obtained from the laws of conservation of fluxes of mass, momentum, and energy under the assumption that $P_2 - P_1$ is small compared to the values P_1 and P_2 before and after the wavefront. The width of the wavefront is

$$\delta = \frac{8aV^2}{(P_2 - P_1)(\partial^2 V/\partial P^2)_S}\,. \tag{5.5}$$

Here $V = \rho^{-1}$ is the specific volume; the kinematic coefficient

$$a = \frac{\nu + \chi(\gamma - 1)}{2C_{\rm L}^3} \tag{5.6}$$

is determined by the speed of sound $C_{\rm L}$, the kinematic viscosity $\nu = \rho^{-1}\left[(4/3)\eta + \xi\right]$ (with η and ξ the coefficients of viscosity of an isotropic medium), and the density ρ; $\chi = K/(\rho C_P)$ is the thermal diffusivity, which is determined from the thermal conductivity K and the constant-pressure heat capacity C_p; and $\gamma = C_p/C_V$ is the adiabatic exponent. The drift flux $I_{\rm dr} = \rho v$ is ensured by the movement of atoms in the SW field with a velocity $v = -\mu\nabla P$, where μ is the mobility. Using the explicit expression for the curvature of the polytropic curve, $(\partial^2 V/\partial P^2)_S$, we arrive at the following expression for the effective diffusion coefficient D, which links the total flux $I = I_{\rm dr} + I_{\rm dif}$ (with $I_{\rm dif}$ the diffusion flux) and the concentration gradient ∇C:

$$D = D_0 + \frac{\rho\mu}{8}\,\frac{\gamma+1}{\gamma^2}\,\frac{C_{\rm L}}{\nu + \chi(\gamma-1)}\,\frac{C_{\rm L}^2}{PV}\,\frac{(P_2 - P_1)^2}{P}\,|\nabla C|^{-1}\,, \tag{5.7}$$

where the initial diffusion coefficient is determined by the Einstein – Smoluchowski formula $D_0 = \rho\mu T/\Omega$ (here Ω is the atomic volume and T is the temperature in energy units). The expression for the normalized diffusion coefficient is

$$\frac{\Delta D}{D_0} = \frac{D - D_0}{D_0} = \frac{1}{8}\,\frac{\gamma+1}{\gamma^2}\,\frac{\rho C_{\rm L}^3}{\nu + \chi(\gamma-1)}\,\frac{P_2 - P_1}{P^2}\,\frac{L}{C_0}\,\frac{\Omega}{T}\,. \tag{5.8}$$

Here we have used the estimate $|\nabla C| \sim C_0/L$, with C_0 the concentration of tracer atoms at the surface and L the depth of penetration of these atoms after the SW wave has passed. According to (5.8), the increase in mass transport is ensured not only by the pressure drop $P_2 - P_1$ but also by the decrease of the kinematic coefficient (5.6), a decrease caused by the reduction of viscosity ν and thermal diffusivity χ under a rise in pressure. For typical values of the quantities involved ($\rho \sim 1 - 10$ g cm^{-3}, $\gamma = 5/3$, $\Omega \sim 10^{-23}$ cm^3, $C_0 = 10^{-1} - 1$, $L \sim 10^{-5}$ cm, and $T \sim 10^{-14}$ erg), the condition $\Delta D \gg D_0$ yields the following inequality:

$$\frac{(P_2 - P_1)^2}{P_2^2} \gg (10^{-2} - 1)\left[\nu + \chi(\gamma - 1)\right]. \tag{5.9}$$

Inequality (5.9) holds even for a small drop in pressure in the SW, provided the wave substantially reduces the viscosity. Actually, the factors that are important here are the magnitude of the pressure and the pressure gradient, which reduce the value of the kinematic coefficient. Hence, another possible mechanism of mass transport, which in contrast to the mechanism discussed in Section 5.1 is of an athermal nature, is a shock wave. Such a wave is capable of causing an enhanced migration of atoms at great depths, where thermal diffusion processes contribute nothing. The intensity of mass transport is determined not only by the pressure amplitude in the SW but also by the spatial pressure gradient, which,

depending on the initial profile of the shock wave (determined by irradiation), may increase. This conclusion is in good agreement with the kinetic model of defect formation in the field of a shock wave (see Section 3.4).

6. Generation of elastoplastic waves in metals due to high-power pulsed beams of charged particles

The effect of HIB on solids is accompanied by solid-, liquid-, and gas-phase processes. When the duration of irradiation is roughly 100 ns, at intensities $I \leqslant 10^8$ W cm^{-2} solid-phase processes dominate; at $I \geqslant 10^{10}$ W cm^{-2}, the gas-phase and plasma processes dominate; and in the medium range of 10^8 – 10^{10} W cm^{-2}, all three processes run simultaneously. It is for the medium range of intensities that we are forced to determine the contribution of each process to the overall interaction effect.

Detailed experimental and theoretical investigations into the problem of generation of elastoplastic waves in aluminum, copper, and lead targets subjected to HIB irradiation from a TONUS accelerator were conducted by Chistyakov et al. [122], who also found some characteristics of ablation plasma. The maximum intensity with targets 0.2 to 1 cm thick reached $\sim 2 \times 10^8$ W cm^{-2} for a 6 to 10 cm^2 cross-sectional area of the beam. The different sublimation energies of metals lead to markedly different conditions of formation of a plasma layer on the target's surface and, as a result, to different values of the parameters of the generated waves. A voltage pulse was detected by an aperiodic piezoelectric transducer (with a resolution of $\sim 10^{-8}$ s) placed at the rear (unirradiated) surface. The recoil impulse was measured by a ballistic pendulum, and the amount of mass carried away, by weighing. The dynamics of plasma spread was recorded by an optoelectronic camera. The amplitudes of the signals from the piezoelectric gages were proportional to the beam's current density. The pictures taken by a streak camera revealed that the plasma spread velocity $v_{\rm pl}$ increases with the irradiation intensity. Table 3 lists the results of experiments and calculations: the mass Δm carried away in the course of one pulse, and the recoil impulse J. The values of $v_{\rm pl}$ estimated by the formula $v_{\rm pl} = J/\Delta m$ varied within the interval $(1-8) \times 10^3$ m s^{-1}. Clearly, Δm correlates with the sublimation energy $E_{\rm s}$ of the metals: 0.96 kJ g^{-1} (Pb), 4.8 kJ g^{-1} (Cu), and 9.8 kJ g^{-1} (Al), i.e., the smaller values of $E_{\rm s}$ correspond to the larger values of Δm.

Table 3. Experimental and theoretical values of the mass Δm carried away and the recoil impulse J when the target is HIB irradiated (0.2 – 0.6 MeV, 100 ns, 1500 A cm^{-2}).

Target	Sublimation energy	Experiment		Theory	
	$E_{\rm s}$, kJ g^{-1}	Δm, mg	J, N s	Δm, mg	J, N s
Al	9.8	0.45	3×10^{-3}	1.7	2.2×10^{-3}
Cu	4.8	1.2	1.5×10^{-3}	1.5	1.9×10^{-3}
Pb	0.96	16.9	1.3×10^{-2}	18.4	1.3×10^{-2}

The process is described by a system of equations containing the kinetic equation of particle transport, the equations of the continuum mechanics, and a wide-range equation of state. When $I \leqslant 10^{13}$ W cm^{-2}, we can ignore electron and radiant heat conduction [123]. In all cases the electrical conductivity of the medium σ was found to exceed $10^4\,\Omega^{-1}$ m^{-1}, so that one can ignore the effect of the electric field (whose strength is proportional to j/σ) on particle transport, while the Coulomb force acting on the beam particles is much weaker than the friction force, which determines the specific energy loss by the particles. In order to solve the problem, Wood and Giles [124] employed the elastoplastic model, in which the same equations describe processes within the region where energy is deposited (where the matter can melt and evaporate) and outside that region. The equations of the continuum mechanics for the case of one-dimensional geometry with bulk energy release taken into account have the following form:

$$p\,\frac{\mathrm{d}z}{\mathrm{d}t} = \frac{\partial \Sigma}{\partial z}\,, \tag{6.1}$$

$$\frac{1}{V}\,\frac{\mathrm{d}V}{\mathrm{d}t} = \frac{\partial v}{\partial z}\,, \tag{6.2}$$

$$\frac{\mathrm{d}u}{\mathrm{d}t} - VS_z\,\frac{\mathrm{d}\Sigma_z}{\mathrm{d}t} + (p+q)\,\frac{\mathrm{d}V}{\mathrm{d}t} = D\,, \tag{6.3}$$

$$\frac{\mathrm{d}S_z}{\mathrm{d}t} = 2\mu\left(\frac{\mathrm{d}\Sigma_z}{\mathrm{d}t} - \frac{1}{3V}\,\mathrm{d}t\right), \tag{6.4}$$

$$\frac{\mathrm{d}S_x}{\mathrm{d}t} = \frac{\mathrm{d}S_y}{\mathrm{d}t} = 2\mu\left(-\frac{1}{3V}\,\frac{\mathrm{d}V}{\mathrm{d}t}\right). \tag{6.5}$$

Here v, ρ, V, and u are the velocity, mass density, specific volume, and the internal energy of the substance; z is the spatial coordinate; $\Sigma = S_z - (p+q)$ is the total stress; S_x, S_y, and S_z are the components of the stress deviator; μ is Lamé's constant; p is the hydrostatic pressure; q is the artificial viscosity; $\mathrm{d}\Sigma_z/\mathrm{d}t = \partial v/\partial z$ is the deformation rate; and D is the energy deposition function (the amount of energy released in unit mass per unit time during the passage of particles through matter). Plastic flow is described by the law of conservation of the stress deviator at the yield point, whereby the system of equations was augmented with the von Mises yield criterion $S_x^2 + S_y^2 + S_z^2 \leqslant (2/3)\,Y_0^2$, where Y_0 is the yield stress in uniaxial tension. The system of equations incorporated the equations of state, which allowed for phase transformations in the energy deposition zone [125] and was solved by Wilkins's method [126] with linear artificial viscosity. The program was tested on the existing self-similar solutions of problems of a gas expanding into a vacuum, sound propagation in a gas, collision of solids, and decay of an arbitrary discontinuity in a gas.

The energy deposition function was calculated via the differential flux density of particles in matter by the multistage method [127]. The stopping properties of matter for electrons were determined by the Bethe – Bloch formula and for ions, from tabulated data in [68]. The carried-away mass and the recoil impulse were calculated by the formulas

$$\Delta m = \lim_{t\to\infty}\left(S_{\rm b}\int_{z_{\rm q}}^{z^*}\rho(z)\,\mathrm{d}z\right), \tag{6.6}$$

$$J = \lim_{t\to\infty}\left(S_{\rm b}\int_{z_{\rm q}}^{z^*}v(z)\rho(z)\,\mathrm{d}z\right), \tag{6.7}$$

where $S_{\rm b}$ is the beam's cross-sectional area, $z_{\rm q}$ is the coordinate of the plasma's free surface, and z^* is the coordinate of the plane bounding the fraction of the plasma carried away. The results of computer simulation and the experimental data are compared in Table 3. Since z^* cannot be found precisely by only solving equations (6.6) and (6.7), it

was assumed that that fraction of the target mass was carried away that had a density $\rho \leqslant \rho(z^*)$. Analysis of the calculated distributions $\rho(z)$ showed that the mass density of the plasma jet rapidly decreases as we move closer to the free surface and that this region with a low density has a velocity that exceeds the mass velocity of the medium by a factor of ten if $\rho > \rho(z^*)$. The value of z^* was chosen from the condition that $\rho(z^*) = 0.01\rho_0$, where ρ_0 is the initial density of the substance. Then equations (6.6) and (6.7) yield values of Δm and J close to the experimental values, which corroborates the validity of the model.

The general laws that govern the generation of stress waves in the solid fraction of the target irradiated either with electron beams or with ion beams depend primarily on the energy deposition function. For this reason we compare the distributions $D(z)$ normalized to a single incident particle for different materials. For particle energies of about 0.5 MeV the ion ranges are approximately a hundred times shorter than the electron ranges, so that the width of the energy deposition zone for ions is also smaller by a factor of 100 than the size of the zone for electrons. Then, at equal HEB and HIB fluences the amplitude of the stress waves may differ substantially. Chistjakov et al. [128] studied the role of the plasma jet in the generation of stress waves. For $j \leqslant 1$ kA cm^{-2}, a compression wave is generated in the solid portion of the target, while directly behind the compression wave there is a rarefaction wave, which is generated as a result of reflection of the compression wave from the irradiated surface. As j increases, matter in the energy deposition zone begins to rapidly evaporate, and, as a result of the recoil impulse being transferred to the target, the irradiated surface ceases to be free. The result is a reduction in the magnitude of the tensile stresses and their total disappearance. This result was also corroborated by Chistyakov et al. [122]. In the event of irradiation with ions with the same energy (0.5 MeV), due to the high density of energy release, already at $j \geqslant 20$ A cm^{-2} an ablation plasma is produced, which generates only compression waves.

The possible mechanisms of generation of elastoplastic waves clearly manifest themselves in HIB irradiation of metals. At different moments in time, the stress fields exhibit a two-wave structure, which can be explained by the difference in the mechanism of generation of the components of this structure. At the beginning of irradiation, a thermoelastic wave is generated in the solid phase of the absorption layer. When melting is ceased, the stresses decrease, with the result that the trailing edge of the wave is formed. Further heating of the melt with the beam increases the pressure, which 'splashes' the substance in the direction of the free surface accompanied by stress unloading in the direction of the unirradiated solid fraction of the target. This unloading generates a new compression wave in the solid. The two-wave structure of the wave explains the complicated shape of the oscillograms recorded by piezoelectric gages. No two-wave structure is observed when the target is irradiated with electrons, since due to the large width of the energy deposition zone the thermoelastic wave has not enough time to perceptibly leave the region where such a structure is formed before the substance has melted.

With allowance for the mechanism of wave generation we have just described, the estimate of the initial width of the stress wave is

$$\Delta x_0 = R_0 + C_L \tau_p \,, \tag{6.8}$$

where R_0, C_L, and τ_p are the projected range of the particles, the velocity of longitudinal sound, and the length of the irradiation pulse, respectively. In the event of HIB irradiation, $C_L\tau_p \gg R_0$, so that Δx_0 is determined solely by the pulse length τ_p. When a high-current electron beam irradiates the target, $R_0 \gg C_L\tau_p$, so that Δx_0 depends on the energy E of the beam electrons. We believe that the validity of estimate (6.8) is corroborated by the results of computer simulation. For instance, an increase in E by a factor of two doubles Δx_0, while in the event of HIB irradiation the width of the wave changes insignificantly. Let us analyze the effect of the parameters of HEB and HIB irradiation on the amplitude of the compression stresses. For HEB irradiation, the energy deposition zone is large, and stress unloading in the direction of the solid fraction of the target proceeds within a time $t \gg \tau_p$. Hence, the stress amplitude is determined only by the values of j and τ_p. An increase in E does not lead to a sizable increase in the wave amplitude. When ions are used, the 'splashing' of matter in the narrow energy deposition zone proceeds simultaneously with the heating of the target, whereby, notwithstanding the high energy release density, the wave amplitude remains moderate. An increase in the ion energy and, hence, in the width of the energy deposition zone increases the plasma 'splashing' time, which substantially increases the wave amplitude.

The given results show that in the cases of both HEB and HIB irradiation, in the given intensity range, the temperature of the medium outside the energy deposition zone changes insignificantly ($\leqslant 10$ K). Hence, in the unirradiated region all the structural and phase transitions are initiated only due to the propagation of stress waves. However, these results were obtained for thick targets (~ 1 cm) and cannot be used to extract information about the characteristics of the waves at small depths (less than 1 mm), where the intensity of the transitions is the highest.

7. Synthesis of thin films and ultradisperse powders using high-power beams of charged particles

One of the effects of the interaction of concentrated pulsed radiative energy fluxes and solids is the ablation (ejection) of matter, which is caused by the rapid heating of matter in the radiation absorption region and the transformation of such matter into a plasma – vapor state. The effect was detected in laser irradiation [127 – 131] and in HEB [4] and HIB [29, 71] irradiation. It has been observed with beams of nanosecond and microsecond pulse lengths at intensities and fluences exceeding certain threshold values. Ablation plasma (AP) is successfully used for manufacturing thin films and coatings by depositing the plasma on special substrates, in the synthesis of nanosized ultradisperse powders, and in a new method of diagnosing the characteristics of concentrated energy fluxes. Hence, the study of the laws governing AP formation is of great scientific and practical interest.

7.1 General laws of the ablation process

The characteristics of ablation plasma generated by applying pulsed light from a laser to metals have been thoroughly studied over a broad range of intensities (up to 10^{14} W cm^{-2}) [129 – 134]. However, the theoretical description of the phenomenon and the very method of producing such plasma encounter formidable difficulties, a fact noted by Steverding et al. [4], who were the first to observe and study AP in the case

of HEB irradiation of metals. There are two advantages of using HEB in comparison to lasers:

(1) The possibility of irradiating large areas (several tens of square centimeters) with a beam with a uniformly distributed intensity up to 10^{11} W cm^{-2} and the fact that electron ranges are considerably shorter than the diameter of the beam spot make it possible to formulate and solve a one-dimensional problem, while for narrow beams of laser light this can hardly be done.

(2) It is much more easy to analytically describe electron absorption than the absorption of low-energy photons. To the first approximation, the cross section of electron scattering in the target can be assumed constant for HEB pulse lengths of several tens of nanoseconds, while due to the rapid increase of the scattering cross section for low-energy photons directly in the course of laser action, the photon penetration depth decreases by several orders of magnitude. Since the deposited-energy profile determines the subsequent hydrodynamic flow of the plasma-vapor matter, the precise knowledge of this profile is important if we want to develop quantitative theories.

HEB irradiation (2 MeV, 30 ns, fluences Φ up to 400 J cm^{-2} per pulse) of thin (0.03 – 1 mm) copper plates is accompanied by ablation of copper in the plasma-vapor state [4]. The dynamics of the process was recorded by a high-speed camera. The main results of the observations are as follows: the ejection of matter from the surface occurs in a compact manner (in the form of a plate), and the rate of ejection is constant under irradiation but exceeds the thermal velocity of the particles (the difference increases with Φ). No gap between the ejection matter and the target was observed. Finally, the ejection occurs along the normal to the surface, irrespective of the direction of the beam. As Φ increased from 40 to 250 J cm^{-2} per pulse, the ejection rates increased from 1800 to 5000 m s^{-1}, and for equal fluences a large spread was observed in the values of these rates, which the researchers explained by the nonuniform radial distribution of energy in the beam (the $1/r^2$ law) and by energy fluctuations, which reached 15% of the average value. At fluences higher than 60 J cm^{-2} per pulse, ejection of matter from the back of the target (i.e., the unirradiated part) was also observed and the process was found to have the same characteristics as that on the irradiated surface. This process was also accompanied by brittle fracture of the sample, in which a main longitudinal crack developed. The thickness of the ejection was found to increase with T, and the rate of expansion of the plasma cloud, v, was found to depend on the plasma temperature according to the law $v \sim T^{1/2}$.

The rate of ablation of the particles was calculated in the following way. Due to the very short length of the pulses in the beam and the inertia of target's material, the rapid heating of this material in the irradiated region creates a compression pulse, whose initial profile corresponds to the distribution of the absorbed dose with a peak at a depth of roughly 0.2 mm. This pulse propagates in the form of a shock wave into the bulk of the target and toward the irradiated surface. When it is reflected by this surface, it is transformed into a pulse of tension. As a result of a linear combination of these pulses, the surface layer is under a double load and starts to move with a velocity that is approximately twice the particle velocity in the compression pulse, u. Using the equations for SW propagation, the Grüneisen equation, and the equation of state and estimating the mean thermal velocity of the particles v by the well-known formula of statistical thermodynamics, Steverding et al. [4] found that

$$\frac{u^2}{v^2} = \frac{\pi \mu c_V}{4R}\,, \tag{7.1}$$

where R is the gas constant, μ is the molar weight, and c_V the specific heat capacity at constant volume. As the temperature rises, c_V rapidly increases, and $u \gg v$. This explains the following experimental fact: although laser irradiation generates a temperature of several electronvolts, the velocity of injected ions in the AP reaches several kiloelectronvolts [4]. The given theory provides a good description of the characteristics of the AP produced by laser light and HEB.

Metals irradiated with high-power ion beams revealed the same general laws governing the ablation process as in laser and electron irradiation. However, for equal fluences and intensities of HIB and HEB and equal particle energies, the ion ranges are several orders of magnitude shorter than electron ranges, with the result that the heating rates are higher in the case of ions, and this intensified ablation.

In their research, Yatsui et al. [30, 32, 34, 35, 82, 135] obtained, via experiments and theoretical studies, reliable formulas linking the AP parameters and the characteristics of thin films. The entire process was found to consist of two consecutive stages: the evaporation of matter from the surface in the form of an expanding dense plasma-vapor cloud interacting with the beam, and the subsequent adiabatic expansion of the plasma into vacuum and its deposition onto the substrate. The thickness of the evaporated layer was assumed to be equal to the thickness of the layer heated by HIB at a constant rate of evaporation of that layer. The behavior of the plasma was described by a one-dimensional hydrodynamic model, which incorporates the continuity equation (7.2), equations (7.3) and (7.4) for the momentum and energy (respectively), and the equation of state (7.5):

$$\frac{\partial \rho}{\partial t} + \rho \frac{\partial v}{\partial x} + v \frac{\partial \rho}{\partial x} = 0\,, \tag{7.2}$$

$$\frac{\partial v}{\partial t} + v \frac{\partial v}{\partial x} + \frac{1}{\rho} \frac{\partial \rho}{\partial x} = 0\,, \tag{7.3}$$

$$\frac{\partial e}{\partial t} + v \frac{\partial e}{\partial x} + \frac{P}{\rho} \frac{\partial v}{\partial x} = \varepsilon(1+\alpha) t^{\alpha}\,, \tag{7.4}$$

$$P = (\gamma - 1)\rho e\,, \tag{7.5}$$

where $\rho, v, P, e, x(\geqslant 0), t$, and γ are the mass density, velocity, pressure, specific energy, coordinate, time, and the ratio of specific heat capacities, respectively. The constants ε and α were chosen in such a way that the right-hand side of (7.5) represented the instantaneous absorbed power per unit mass of the expanding material: $\varepsilon \sim I/(R\rho_0)$, where I is the irradiation intensity, R is the ion range, and ρ_0 is the initial density. If $\alpha = -1$, no energy is absorbed (the case of adiabatic expansion) when $t > \tau_p$, where τ_p is the length of the irradiation pulse; $\alpha = 0$ corresponds to absorption of energy at a constant rate; and at $\alpha = 1$, this rate linearly increases with time. The solution of equations (7.2) – (7.5) leads to expressions for the functions $\rho(x,t)$ and $v(x,t)$, the density of the ion current in the plasma $I_B(x,t) \sim \rho v$, and to estimates of the temperature T_0 corresponding to the maximum value of I_B.

Irradiation was done on an ETIGO-II accelerator with protons (> 80%) and carbon ions (1.2 – 1.6 MeV, 70 ns, 1000 A cm^{-2}, 10^8 W cm^{-2}, 25 J cm^{-2} per pulse). The Ti and

Al targets were positioned at an angle of 45° with respect to the beam axis at a distance of 37 mm from the substrate. It was found that $T_0 \sim 1.6-2$ eV; $I_{B,max} \sim 500$ A cm^{-2} for Ti and 400 A cm^{-2} for Al. The experiments showed that the plasma density n and temperature strongly depend on time (for $t < \tau_p$) and position and vary within broad limits from 10^{18} to 5×10^{22} cm^{-3} and 0.3–20 eV, respectively, with $n \propto T$. The calculated values of T_0 and I_B also strongly depend on the rate of energy absorption and τ_p and weakly depend on α. The degree of plasma expansion near the target's surface under irradiation is much smaller than for adiabatic expansion. The different experimental and calculated functions $I_B(t)$ at the substrate surface for different accelerating voltages (energies) of the beam ions are in good agreement (Fig. 17), which is proof of the validity of the adopted model. The observed increase in the discrepancy between them at earlier stages is probably due to the recombination of ions in the plasma, which is ignored by the model. More recent experiments of Kang et al. [136] established that the temperature T_0 and the energy E_d per evaporated atom are linear functions of Φ (up to 80 J cm^{-2} per pulse; here $E_d = 3-15$ eV per atom).

The same researchers established the dynamics of the conversion of the thermal energy of the AP into the kinetic energy of the AP by calculating the time dependence of the plasma temperature at the target surface, $T(t, x = 0)$, the dynamic and static pressures, $P_d \sim \rho v^2/2$ and P [see (7.5)], at different distances x from the targets [137]. They used the same equations in the case of a linear input of energy by the beam ($\alpha = 0$), which is closest to the real irradiation regime, for $I \sim 10^9$ W cm^{-2}. The calculated dependence $T(t, x = 0)$ for the Ti target shows that in the first stage of heating and evaporation the temperature very rapidly (in about 70 ns) reaches its maximum $T_{max} \sim 1.6$ eV. Then, in the second stage of adiabatic expansion, the plasma is rapidly cooled (to $T_{max}/2 \sim 0.8$ eV in roughly 1 μs), with a fraction of the thermal energy of the particles converted to their kinetic energy. The maximum value of P_d at $x = 3$ cm amounted to roughly 1.4×10^7 Pa and was reached in $t \sim 2$ μs. This value is approximately ten times larger than the static pressure, i.e., the kinetic energy of the plasma is much higher than the plasma's thermal energy.

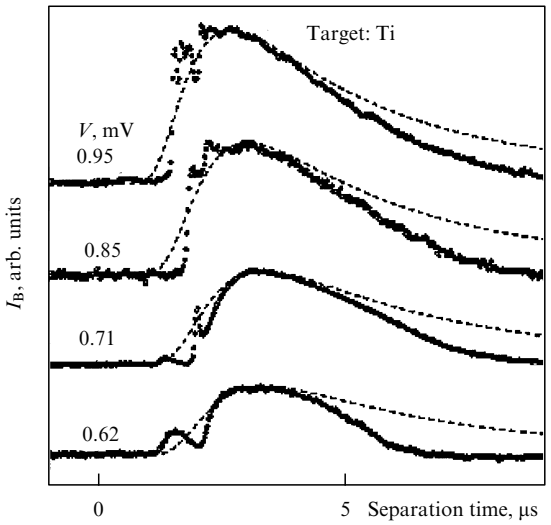

Figure 17. Time dependence of the ion current of the ablation plasma produced as a result of HIB irradiation (protons > 80% and carbon ions; 1.2–1.6 MeV; 70 ns) of a Ti target for different values of the accelerating voltage across the diode: the solid curves correspond to the experimental data and the dashed curves, to the results of calculations.

7.2 Production of thin film

To produce thin films (TF), the plasma was deposited on special substrates without heating them to any noticeable extent, which allowed the exclusion of unacceptable temperature changes in the structure and composition of the film and substrate materials. The use of HEB and HIB to produce AP with irradiation of nonradiative targets has certain advantages over the use of laser beams:

(1) The large coefficient of beam absorption.

(2) The fact that the radiation is absorbed in the bulk of the target, which makes it possible to avoid unacceptable overheating of the target material and to produce a more uniform depth distribution of temperature, which excludes intense absorption of the radiation in the thin melted layer of the target leading to flashing, a feature characteristic of laser irradiation. The bulk nature of absorption also makes it possible to substantially increase the mass of the AP (say, for HIB irradiation the average amount of the material removed is 1000 times larger than for laser irradiation [138, 139]). This allows using deposition rates (~ 1 cm s^{-1}) that are several orders of magnitude higher than those attained by all other methods.

(3) Large areas of irradiation.

(4) The possibility of developing a one-dimensional model of the process and of providing a more exact description of the particle–target interaction.

(5) Essentially higher efficiencies, in view of which the cost per unit energy with HIB irradiation is smaller than with laser irradiation.

Estimates also yield low costs of producing 1-μm thick films (US$5 per square meter) [17]. These beams found wide (and successful) use in the technology of TF synthesis. The Japanese technology known as Ion Beam Evaporation (IBE) makes it possible to manufacture thin films with special properties, including multilayer films of high-temperature superconducting materials for the microsystems of the electronic and optical industries [32, 34]. IBE provides the possibility of producing thick films, including films manufactured from high-melting metals, of forming amorphous and crystalline layers with a given structure, of sputtering ceramic materials onto metals, and of synthesizing nanosized ultradisperse powders. IBE has been used as a base for producing diamond-like coatings [17, 32, 140, 141]. The IBE technology could be used in medicine to deposit thin films on the surfaces of implanted fasteners with aluminum, e.g., films of hydroxylapatite, the main inorganic component in the bones of humans and animals [142].

It was found that the characteristics of thin films produced by irradiation differ from those produced by vacuum deposition or sputtering. By properly selecting the material of the sputtered target, the irradiation regimes, the composition and parameters of the irradiation medium, the substrate material, and the subsequent thin-film annealing, it became possible to produce films with elevated mechanical strength and special electric, magnetic, and optical properties. Here, we analyze the experimental results of studies of the laws governing thin-film formation that we believe to be the most important. Beams of light ions (protons, carbon, nitrogen, etc.) were used for irradiation, since, first, such ions have ranges that are longer than those of heavy ions and,

second, they can be produced more easily. To date, the IBE technology has been used to synthesize films from various materials: metals (Al, Pb, Mo, W, Ti, Au, Fe, Zn, Cu, and Nb), ceramic materials (BN, SiC, $YBa_2Cu_3O_{7-x}$, ZrO_2, and AN), and insulators (B, C, ZnS, ZnS + Mn, and $BaTiO_3$), including apatites. Figure 18 depicts two schemes of thin-film deposition on a substrate for frontside (FS) and backside (BS) configurations. The latter came into use only recently and will be examined later. The high-power ion beam struck the target at an angle of 45° (Fig. 18a). The substrate was mounted on a holder below or above the target in such a way that its surface was kept parallel to the irradiated surface of the target, which ensured uniform deposition (with respect to depth) of the film. With the geometries used in these experiments, one-third (on average) of the sputtered material landed on the substrate, with a fraction of the material passing around the substrate, as photographs of the process clearly indicate. Deposition was done in vacuum ($10^{-4}-10^{-5}$ Torr) with an insignificant amount of impurities in the residual gases. Then, with the low concentration of these impurities in the substrates, the purity of the films was extremely high.

Davis et al. [36] used HIB (350 – 50 keV, 30 kA, 0.4 μs) containing H^+, C^+, C^{++}, and O^{++} ions to produce thin films by irradiating titanium and graphite. They found that there is a threshold in the absorbed energy density corresponding to a definite fluence, which for Ti and graphite amounted to 5 and 12 J cm^{-2} per pulse, respectively. The energy spectrum of the beam particles was assumed constant during irradiation. The temperature field in the target was determined by numerically solving a one-dimensional heat conduction equation for a constant density of the material and varying values of the heat capacity and thermal conductivity. The equation incorporated a heat source, which reflected the real input of energy determined from the oscillograms of the beam's current and voltage. The hydrodynamic flow of the material and the losses to radiation were ignored. The target temperature in the ablation process was assumed equal to the boiling point. Only the solid – vapor phase transition was taken into account, which is a fully valid approach only for graphite. Strictly speaking, in metals one must take into account the latent heat of both melting and evaporation, but the latter is much larger than the former (say, for Ti by a factor of 15). At the threshold value of Φ, the ablation mass changes suddenly from zero to the mass of the layer corresponding to the range of the beam ions. The following functions of Φ have been found through experiments: (a) the ratio of the ablation layer thickness to the beam absorption depth, (b) the ratio of the energy spent on ablation to the incident energy, (c) the threshold absorption energy E_a per atom needed for ablation to begin (4 eV for Ti and 7 eV for graphite), and (d) the depth dependence of E_a in the beam absorption region.

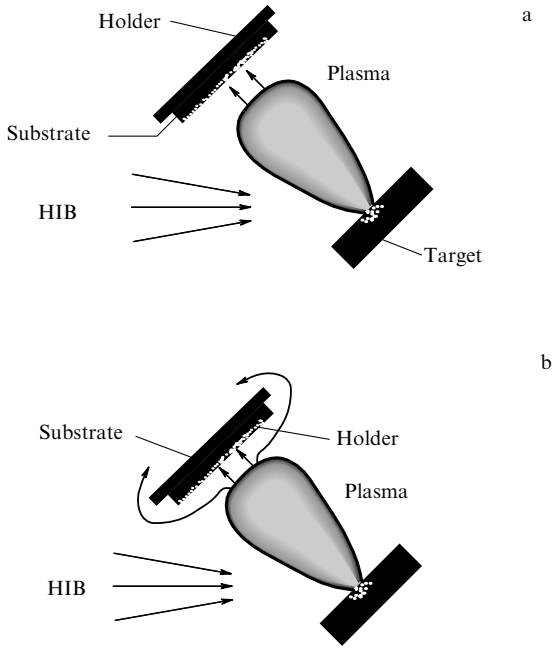

Figure 18. Deposition of a thin film produced by HIB irradiation: (a) frontside (IBE/FS) and (b) backside (IBE/BS) configurations.

Specific features characteristic of the production of films of ZnS, $YBa_2Cu_3O_{7-x}$, $BaTiO_3$, ZrO_2, and Al involving the use of the same accelerator (ETIGO-II) have been noted by Yatsui et al. [16, 32], Shimotori et al. [29], Muller and Schultheiss [142], Sonegawa et al. [143], and Kamihata et al. [144]. In the plasma deposition using a target of ZnS with a cubic structure onto a glass substrate, a thin film formed had a hexagonal structure. The thickness of this film was found to linearly increase with the number of irradiation pulses [16, 29]. After Mn was added as a color center, it became a component of the multilayer produced by consecutive deposition from the plasma of layers of $BaTiO_3$, ZnS : Mn, Ta_2O_5, HfO_2, and Al onto the indium – titanium oxide (ITO) covered by glass [16]. This multilayer was used in electroluminescent devices and produced a strong (up to 105 cd cm^{-2}) orange yellow color.

When $YBa_2Cu_3O_{7-x}$ and MgO(100) were used as target and substrate, respectively, no crystallinity in the film was discovered [16, 32]. However, after annealing (2 h at 985 °C followed by 10 h at 485 °C in oxygen), crystallinity with a well-defined orientation along the *c* axis emerged. Oxygen pressure had a strong effect on the resistance of the film and on the temperature dependence of that resistance.

Changes in crystallinity and stoichiometric composition were observed in thin films produced by irradiating a target that had the composition (mol %) of 92.7 $BaTiO_3$, 4.5 TiO_2, 2.6 Nd_2O_3, 0.1 Bi_2O_3, and 0.1 MnCo in the event of deposition on an Si(100) target covered by aluminum. The structural and phase composition was determined mainly by the Ti/Ba concentration ratio, which depended on the number of pulses [16, 32]. The film deposited on an Si(100) substrate from a BN target with a hexagonal structure (h-BN) retained this structure at low irradiation intensities, while at elevated intensities an additional cubic structure was found to emerge [16, 32]. The addition of Y_2O_3 to a target of monoclinic ZrO_2 in the formation of thin films on the Si(100) substrate was also found to affect the structure of the film. If its content amounted to 1.1 – 4.5 mol %, a tetragonal structure emerged, while if the content was 7 – 12 mol %, the structure became cubic [32].

Kamihata et al. [144] were able to establish some of the elementary processes responsible for the formation of ablation plasma produced using Pb, Cu, Mo, Ti, Fe, and W targets (which have different sublimation energies). They used an EDIDATRON high-current accelerator (80% H^+, 20% C^+, 400 keV, 50 ns, $j = 20-100$ A cm^{-2}, energy per pulse up to 5 kJ). The angular distribution of the fluence of particles in the ablation plasma has the shape of a cosine curve for all metals. The dependence of the thickness of the

evaporated layer T_a on the normalized absorbed energy E_{abs} is of a threshold nature, with E_{abs} defined as the ratio of the energy absorbed along the range of the beam particles to the energy needed for heating the target to the boiling point. The sudden increase in T_a at $E_{abs} = 1$ discovered for all metals shows that the sublimation energy is the threshold quantity for ablation. This result is in good agreement with those discussed in Section 6, where the contribution of ablation to the generation of elastoplastic waves was studied. There is a strong correlation between the functions $T_a(E_{abs})$ and $T_a(j)$. The observed sudden increase in T_a as a function of j for $j > j_1 = 30$ A cm^{-2} is an indication that j_1 can be assumed to be a threshold value. The function $T_a(j)$ for Pb has a maximum of roughly 0.3 μm at $j = 100$ A cm^{-2}, which is much smaller than the range of the beam particles (~2 μm). For $j > 100$ A cm^{-2}, the value of T_a decreases. The lead ion velocities were varied within a broad interval, $8 \times 10^3 - 6 \times 10^4$ m s^{-1}, at $j = 240$ A cm^{-2} and were found to be much smaller than in the plasma generated by the light from a KrF laser [145].

Rej et al. [139] achieved high rates of deposition of thin films: ~ 30–300 nm per pulse (5–50 cm s^{-1}) were reached by irradiating Cu, Y, Ba, Ag, Al, and carbon on an ANACONDA accelerator (~ 50% H^+, ~ 50% C^+, 150 kJ, 600 keV, 600 ns, and 10–25 J cm^{-2} per pulse). The values were 1000 times larger than those achieved by employing laser light, for equal fluences and intensities of the beams. As the number of pulses increases, nonuniform burst deposition of the film occurred, with the film surface becoming rougher. The researchers explain this fact by impact strain hardening of the target due to the repeated effect of pulses and by the nonuniform distribution of the current density over the beam's cross section, which causes nonuniform heating of the target surface.

Yatsui et al. [32] used a plasma of light ions produced in the irradiation of a target consisting of 90% BN, 5% CaO, and B_2O_3 on an ETIGO-I accelerator (1.2 Mev, 240 kA, 50 ns) for high-dose implantation in Ti of 99.7% purity. For a plasma current density of roughly 1 kA cm^{-2}, the dose of the ions implanted into the target per pulse was roughly 1% of the initial atomic density of Ti, in which formation of the TiN compound was observed. After approximately 20 irradiation pulses, the surface hardness of Ti increased with the number N_p of pulses, and at $N_p = 70$ the hardness became larger by a factor of 1.6 in comparison with the initial hardness.

Two key issues in the technology of film deposition are the possible heating of the film and the presence of impurities. To attain high deposition rates, the substrate is positioned near the target. In the condensation time (~ 10 μs), a layer of about 1 μm thick is formed. The still hot, dense plasma can heat the film through neutralization of the plasma ions and the heat of condensation. This heating has been detected in the deposition of the plasma, produced on an ANACONDA accelerator, onto thin-film metallic resistor substrates. The maximum film temperatures (up to 2000 °C) were reached in depositing carbon on glass [146].

Remnev et al. [147] and Rej et al. [148] analyzed impurities in films produced by irradiating high-purity (99.99%) W and Au with a proton–carbon beam (350–500 keV, 60 ns, $(0.7-1.5) \times 10^8$ W cm^{-2}). Deposition was carried out in a high vacuum with a pressure of the residual gases C, N, and O less than 5×10^{-5} Torr. The concentrations of the same gases in the high-purity GaAs substrate did not exceed 10^{-5}%. Film thicknesses were determined by X-ray fluorescence analysis, and the concentration of carbon and nitrogen in the films was determined by the method of nuclear reactions with 3.1-MeV deuterons and by SIMS. The best results were obtained with predeposition of the films and the use of special cold nitrogen traps [148]. The maximum surface density of the W films was $\sigma_W \sim 1.3$ mg cm^{-2}, with the densities of the impurity elements being $\sigma_C = 9.7$ μg cm^{-2} and $\sigma_N = 0.62$ μg cm^{-2}, and the contents of these elements were (in wt %) $f_C = 0.75\%$ and $f_N = 0.75\%$. For Au these values are $\sigma_{Au} \sim 1.3$ g cm^{-2}, $\sigma_C < 0.2$ μg cm^{-2}, $\sigma_N < 0.1$ μg cm^{-2}, $f_C = 0.1\%$, and $f_N = 0.05\%$. The overall amount of C increased with the number of irradiation pulses (their frequency amounted to 8–10 min^{-1}), which suggested that the films became contaminated by residual gases in the deposition process. Contamination also occurs between the pulses. Remnev et al. [147] and Rej et al. [148] also studied the angular distribution of the fluence of particles in the plasma produced as a result of irradiation of 1-cm^2 disk targets of ZnS, Nb, W, Au, and Pb on a TEMP accelerator (60 ns, 250 A cm^{-2}, 9×10^7 W cm^{-2}, 5 J cm^{-2} per pulse). The distribution was determined by measuring the surface density of these elements on the surface of very thin (0.2–400 nm) films. As in other experiments, the shape of this distribution is close to that of a cosine curve. However, the angular distribution of the film thickness proved to be extremely narrow; the function $\exp(-m\theta)$ is a good approximation of it, with θ being the angle between the chosen direction and the direction normal to the target's surface, and the parameter m varying between 3 and 4.3 for different materials. This shape of the distribution is in sharp contrast to the cosine-curve distribution of the fluence of particles in the evaporated plasma.

Another method that has proved its potential is diamond-like coating (DLC) [17, 32, 140, 141]. For instance, when graphite targets are irradiated with a mixed H/C/O beam (350 keV, 400 ns, 30 J cm^{-2} per pulse) and the plasma is deposited at room temperature on silicon or glass substrates placed at distances of 150 to 225 mm from the targets, the highest rate of film growth is about 25 nm per pulse. Investigation of these films showed that the films consisted of spherical diamond particles about 100 nm in diameter and that the electrical resistance of the films varied from 1 to 100 Ω cm; this is several orders of magnitude higher than the resistance of graphite but is much lower than that of diamond. The use of such films increases the mechanical strength and durability of working pairs in friction units, which makes the application of such films in, say, the aerospace industry effective.

A new method of producing films by the IBE technology has recently been developed in Japan. In contrast to the standard IBE/FS technology (Fig. 18a), in which the injected plasma is deposited on the front side of the substrate, in the IBE/BS technology (Fig. 18b) the plasma is deposited on the back side of the substrate located behind the holder [143]. The film deposition occurs in the diffusion of the plasma through the thin holder. The surface of a $YBa_2Cu_3O_{7-x}$ target was irradiated on an ETIGO-II accelerator (~ 90% protons, 1.1 MeV, 70 ns, 500 A cm^{-2}, 30 J cm^{-2} per pulse, 4×10^8 W cm^{-2}). Si(100), MgO(100), $SrLaGaO_4$(100) substrates were positioned 60 mm from the target. When the IBE/FS method was used, droplike bumps no smaller than 1.5 μm in diameter of yttrium and copper (in the form of an orange peel) were observed on the surface of the film. These bumps appear due to the ejection of drops of the melt from the target.

No such bumps were observed when the film was deposited by the IBE/BS method. Here, the average roughness of the film was 10.35 nm, which is five times smaller than that measured in the IBE/FS method (55.47 nm). Although the deposition rate in the IBE/BS method is roughly 30 nm per pulse, which is ten times lower than in the IBE/FS method, it nevertheless substantially exceeds the deposition rate achieved by laser irradiation. Several differences in the crystallinity of the films have been recorded, which depended on the composition and structure of the substrate material. There are also two other important advantages of the IBE/BS method. First, this method makes it possible to avoid bombarding the film's surface with highly energetic plasma particles (such bombardment reduces the quality of the surface). Second, it increases the purity of films; in particular, it substantially lowers the content of residual gases. The above results corroborate the potential of the IBE/BS technology.

7.3 Synthesis of ultradisperse (nanosized) powders

Ultradisperse powders with grain sizes in the nanometer range can be used in the production of fuel for space vehicles, magnetic plates of Fe, Ni, and Co, magnetic memory devices of huge capacity, substrates for integrating contours manufactured from AlN, high-strength ceramics, and Al_2O_3-based catalysts [30, 136, 149]. In industry such powders are produced primarily by chemical reactions in the liquid phase, but this leads to problems with the composition and chemical purity of the products.

The synthesis of nanosized aluminum powders was investigated by Yatsui et al. [30, 135] and Rej et al. [148]. Plasma produced on an ETIGO-II accelerator is deposited on a steel collector with fine cells, which is placed at different distances from the target, $L = 270-330$ mm, in a chamber containing oxygen under a variable pressure (from 1 to 10 Torr). When the pressure is 1 Torr, the produced powder consists of nanosized spherical aluminum particles with a low content of γ-Al_2O_3, produced as a result of the reaction between Al and O_2. As the pressure increases to 10 Torr, the γ-Al_2O_3 content becomes predominant, while the fraction of Al is small. Varying the temperature of the subsequent annealing between 800 and 1200 °C, the researchers produced powders with different size distributions of particles (5 – 65 nm) and with different fractions of α-Al, δ-Al, and γ-Al [30, 135, 148].

The same researchers produced ultradisperse TiO_2 and TiN powders (see the report in Ref. [150]). The size distribution of the TiO_2 particles was found to depend on L (Fig. 19). For small $L \sim 100$ mm, the vapor in the plasma is too hot for condensation to occur, with the result that the particles are large (up to 2 μm). For large distances ($\sim$300 mm), the vapor cools off, which means that there is enough time for the vapor to become supersaturated, with the condensation of the vapor into fine particles (2 – 50 nm) beginning in the space between the target and the collector.

An analysis of these results prompts the conclusion that notwithstanding the different compositions of the target materials and the different types of irradiation, the production of ablation plasma is characterized by the following general features:

(1) The process occurs under laser, electron, and ion irradiations and exhibits a threshold in the intensity and fluence per irradiation pulse.

(2) The rate of the process is high, with the dynamics represented by two consecutive stages: the ejection of the plasma from the target, and the expansion into vacuum. The velocity with which the plasma is ejected depends on the irradiation regime and is much higher than the thermal velocities of the ions. The concentration and the temperature of a dense (up to 5×10^{22} cm^{-3}) ablation plasma are proportional to the irradiation intensity and fluence.

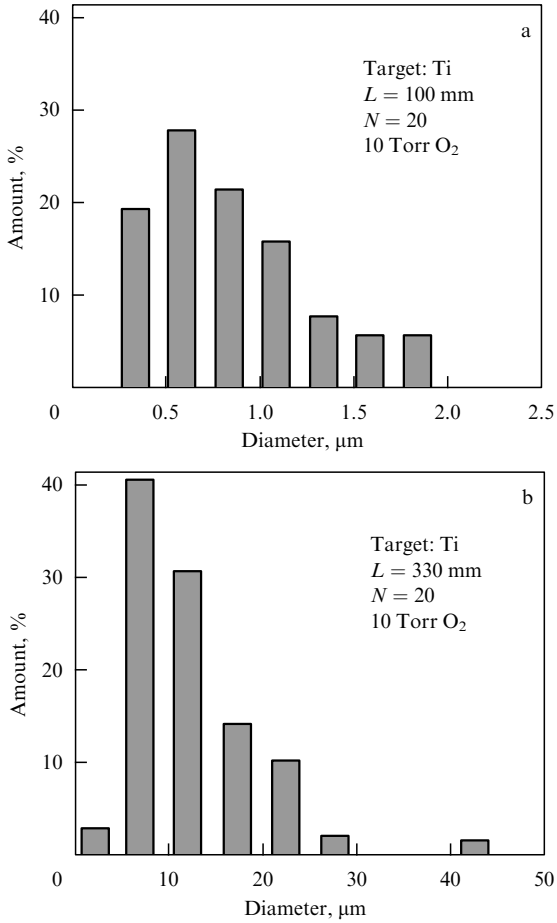

Figure 19. Size distribution of particles of a TiO_2 powder for different distances L between the collector and the target for HIB irradiation on an ETIGO-II accelerator.

The process of formation and the structure of thin films is determined by (a) the type of irradiation and the irradiation regime, (b) the composition and parameters of the medium, (c) the composition of the materials and the structure of the materials of both target and substrate, and (d) the regime of the subsequent annealing of the films. The same factors affect the characteristics of the synthesized ultradisperse nanosized powders.

Of course, problems related to raising the quality of the surface, improving the morphology of the films, increasing their purity, and achieving uniform thickness remain. The IBE/BS technology developed at the Laboratory of Beam Technologies of the Nagaoka University of Technology (Japan) has made it possible to solve some of these problems. Recently, good results have been obtained with special plasma reflectors placed between the target and substrate prior to irradiation, and with special geometric constructions that confine the plasma to the space near the substrate. Another solution is to reduce the mass of the ejected plasma, which can be done by reducing the irradiation fluence and the target thickness. As pointed out by Melic

et al. [151], the same can be achieved (for equal fluences) by the use of heavier ions in the beam, say, Ne^+, which have shorter ranges and reduce the thickness of the ablation layer.

8. Improving the operating characteristics of metals, alloys, and products manufactured from them, using electron and ion beams

An applied problem in studying the modification of materials subjected to high-power beams of charged particles is the improvement of the operating characteristics of end products. In the present review, we describe the basics of, and the prerequisites for, some new radiation technologies. However, there are several reasons why not all of these technologies have been used in industry. Therefore, in this section we present some typical examples of realizing such technologies. When the type and energy of the particles have been chosen, the desired technology can be realized by using a certain combination of intensities and fluences. For instance, when using HIBs whose pulse lengths are about 100 ns to modify the mechanical and tribologic properties of metals, the fluences should not exceed 10 J cm^{-2} per pulse, while in evaporation technologies the fluences are usually 10–50 J cm^{-2} per pulse. In some cases, to increase the processing productivity, special types of accelerators and vacuum chambers were developed. Such devices made it possible to irradiate large areas (up to 1000 cm^2) and, at the same time, to process large number of products [146, 148, 150].

Processing by high-power ion beams improves the electroerosion durability of hermetically sealed reed relays (ferreeds) [152]. The usual way of ensuring low and stable electrical resistance of the contacts in medium- and low-power gas-filled sealed reed relays and resistance to electroerosion is to use gold-based electroplating (the alloys Au/Co, Au/Ni, and Au/Ni/Rh). The report on the results of processing MKA-2701 ferreeds with a double plating of Ni (2-μm thick) and Au (0.5-μm thick) can be found in Ref. [152]. A cartridge containing 250 ferreeds was HIB irradiated ($\sim$50% C^+, $\sim$50% $^+$, 300–400 keV, 100 ns, 20–100 A cm^{-2}). Elemental and phase analysis of the ferreeds showed that the gold layer was mixed with the nickel layer to form a multiphase structure in the surface layer. On–off tests of the ferreeds under a switching voltage $U_s = 60$ V and a current $I_s = 0.08$ A showed an increase in the minimum life of the devices by a factor of four to five in comparison to the case when electrochemical plating was used. The number of switching cycles increased to 10^7, with the ferreed electrical resistance not exceeding 0.05 Ω (in the microwatt switching regime, $U_s = 2 \times 10^{-2}$ V and $I_s = 10^{-2}$ A). It was found that all the electrical parameters of the ferreeds agreed with the specifications and that the yield of rated devices after processing corresponded to international standards.

Goncharenko [153] analyzed the behavior of the stainless steel 12Kh18N10T in acid media (a 1% solution of hydrochloric acid HCl) at room temperature after LHEB irradiation with different numbers N of pulses (from 1 to 100). With a single pulse, craters were found to appear at the location of sulfide and carbide inclusions capable of forming low-melting eutectics. Repeated irradiation, with these detrimental inclusions evaporating, was found to refine the surface, a process accompanied by the formation of a subgrain structure with a grain size of about 100 nm. For $\Phi = 5$ J cm^{-2} per pulse and $N = 100$, the surface frees itself completely of impurities and smooths out, and the craters disappear. The characteristics of

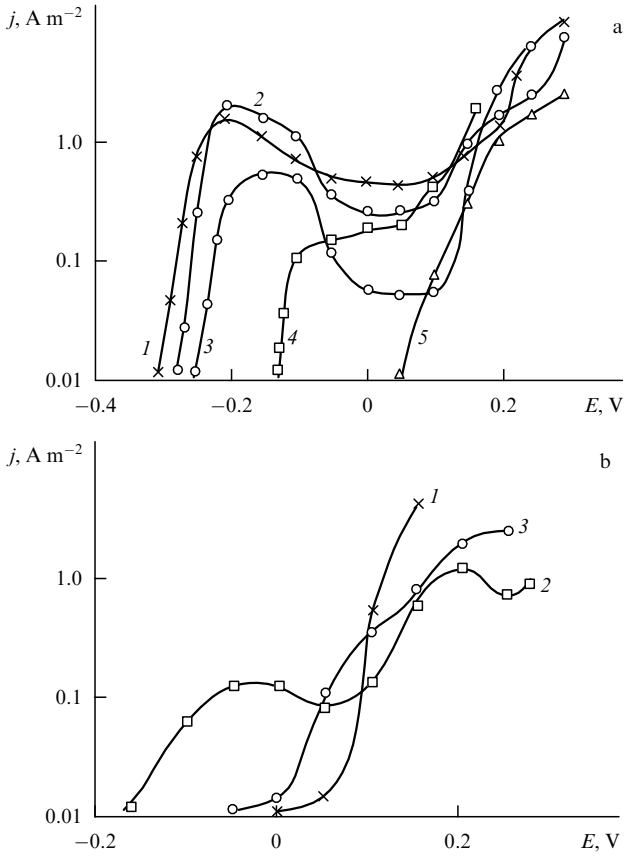

Figure 20. Anode polarization curves for the steel 12Kh18N10T in a 1% solution of HCl after LHEB irradiation in different regimes. (a) Without predeposition of a Ta film: *1*, initial state; *2*, $\Phi = 2$ J cm^{-2} per pulse, the number of pulses $N = 1$; *3*, 5 J cm^{-2} per pulse, $N = 1$; *4*, 5 J cm^{-2} per pulse, $N = 20$; *5*, 5 J cm^{-2} per pulse, $N = 100$. (b) With predeposition of a Ta film (100 nm) and irradiation with a single pulse: *1*, $\Phi = 3.5$ J cm^{-2} per pulse; *2*, 4.5 J cm^{-2} per pulse; *3*, 5.3 J cm^{-2} per pulse.

the anode polarization curves are improved with increasing Φ, since the evaporation rate goes up substantially (Fig. 20a). As N increases, the anode dissolution current decreases with increasing stationary potential. When the latter becomes positive, the dissolution current decreases by a factor of 100 in comparison with the initial current. No substantial redistribution of the impurities (Cr, Ni, and Ti) was detected in the irradiation region. Hence, what is crucial in increasing the corrosion resistance is the cleaning of the surface from detrimental impurities and the formation of a microstructure with a high degree of chemical homogeneity.

Such an effect was accomplished when the surface of the same steel was first coated with a 0.1-μm Ti film and subjected to an LHEB pulse (Fig. 20b). The reason for the increase in corrosion resistance lies in the mixing of titanium and iron accompanied by the transformations described in Section 4. The best processing regime was with a fluence of 3.5 J cm^{-2} per pulse. An increase in the strength properties and corrosion resistance to water vapor was achieved by first applying thin (0.1 μm) high-melting films of Ta, Mo, and V onto the iron surface and then irradiating the new surface with single LHEB pulses [101, 107]. The same results were observed after multiple ($N > 50$) irradiation ($\Phi = 5$ J cm^{-2} per pulse) but without coating the iron surface with a Ta film. As is known, pure tantalum forms a stable, dense, solidly attached oxide layer in oxidizing acids, but its solubility in

iron is too low (less than 0.5%) for a protective layer to form when ordinary methods of fabricating alloys are employed. Mixing, via LHEB irradiation, of Ta with iron produces an amorphous film, which boosts the corrosion resistance.

The study of the effect of HEB and HIB on α-Fe (the base for most types of steels and alloys) has made it possible to determine the optimum processing regimes, which ensure a maximum increase in strength and tribologic properties (see Sections 2 and 3).

An increase in wear resistance upon dry friction has been revealed not only on the surface of HIB irradiated samples of steel, copper, and beryllium but also at depths exceeding the range of the beam ions by several orders of magnitude [10, 69]. The effect occurs because of the formation of a defect structure in the shock wave and the generation of residual compression stresses.

Rej et al. [148] obtained reliable data on the processing of AISI-4620 steel (composition: > 96.3 wt. % Fe, 0.2% C, 0.55% Mn, 1.8% Ni, 0.3% Si, 0.25% Mo, < 0.04% S, < 0.04% P), used in the production of gear transmissions, by varying the values of Φ and N on an ANACONDA accelerator (ions of H, C, and O; 350 keV, 30 kA, 100 ns, one pulse every three minutes). Two inhomogeneous zones were found to form in the surface layer: the melting zone with a thickness of 0.2 to 1 μm and the thermal-affected zone with a thickness of 1 to 1.5 μm. After processing ($\Phi = 5$ J cm^{-2} per pulse, $N = 10$), the Knoop hardness increases by a factor of 1.4, to 466 ± 30 kgf mm^{-2}, which is caused by grain refinement and dislocation formation. The same researchers detected changes in Vickers microhardness after HIB processing of the fast-cutting tool steel R18 (wt. %: 75 Fe, 0.7 C, 4 Cr, 1.8 W, 1 Mo, 1.2 V) used in the manufacture of cutting, boring, and milling tools, on a TEMP technological accelerator (carbon ions, 300 keV, 20 kA, 50 ns, 0.3 Hz). Prior to processing, the samples were quenched from 1270 °C and then tempered at 570 °C in order to produce the martensite phase with the Fe_3W_6C carbides. Rapid annealing by irradiation increased the concentration of point defects and dislocations at the surface. Subsequent treatment (at 455 °C for one hour) was carried out to stabilize the phases. The optimum processing regime, which corresponded to maximum microhardness, was achieved at $\Phi = 1.5$ J cm^{-2} per pulse and $N = 2$. The irradiation ($\Phi = 1.2$ J cm^{-2} per pulse, $N = 5$) of rivets made of U10A steel (> 98% Fe, 1% C, 0.25% Ni, < 0.15% W, < 0.35% Si, < 0.02% P, < 0.02% S) was found to lead to polishing of the rivet surface and to an increase in their service life by a factor of 4.5 [148].

Cutting tools manufactured from tungsten carbide (WC bonded with 5–8% Co) were processed on the TEMP accelerator (1.6 J cm^{-2} per pulse, $N = 1$). As a result, surface roughness decreased from 1.8 to 1.3 μm, but it increased with N. The best processing was achieved in a complex irradiation regime, which consisted of the following stages: (a) a single pulse (~ 0.4 J cm^{-2} per pulse) to clean the surface, (b) several subsequent pulses (~ 0.9 J cm^{-2} per pulse) to reduce crystallization, and (c) several concluding pulses (~ 0.04 J cm^{-2} per pulse) to polish the surface. The best effect was obtained for drills — their service life increased and the quality of the holes was higher. The increase in resistance to wear is due to the increase in the content of the solid solution of W in Co in the surface layer. It was also found that processing by a high-power ion beam increases the resistance to wear of the titanium alloy T14K8 (WC with 14% TiC and 8% Co), which is due to the formation of regions containing nanophase particles of Co_3Ti with grain sizes ranging from 20 to 30 nm [148].

A large-scale technology of HIB processing of cutting tools manufactured from the alloys T5K8 and T5K10 (WC with 5% TiC and 8 and 10% Co, respectively) has been adopted at the automobile plant in Nizhniĭ Novgorod (Russia). Ninety-six cutting tools, which were attached to a turntable placed in the vacuum chamber of the TEMP accelerator, were irradiated simultaneously. Then they subjected to annealing, after which their resistance to wear increased by a factor of 2.8 ± 0.4 [148].

Surface treatment via HIB irradiation of high-melting Ti and Fe–Ni–Cr-based alloys (used in the fabrication of the compressor blades for turbojet engines) [98, 148, 154, 155] was done on TONUS, VERA, TEMP, TEMP-M, MUK, and LUCh accelerators, where the last four were designed for technological purposes. The accelerators ensured irradiation regimes with the following parameters: ions of carbon and 30–40% protons, 100–300 keV, 40–500 A cm^{-2}, 50–100 ns, pulse frequency 0.2–10 Hz, and processed area 60–1000 cm^2. The titanium alloys VT18U, VT9, VT8M, VT25U, and VT33, the nickel alloy EP718ID, the steel EP866Sh, and compressor blades manufactured by the standard technology were tested. After irradiation was completed, the samples and the blades were annealed to achieve structural and phase stabilization of the material in the surface layer. Modifications occur due to the following processes: (a) formation of a gas-plasma cloud; (b) surface melting, gas-dynamic separation of the plasma components, and propagation of a shock wave (for $j > 100$ A cm^{-2}); (c) absorption of the gas into the liquid phase in the course of cooling, high-rate solidification (10^7–10^9 K s^{-1}), and the deposition of the ablation plasma components onto the surface after irradiation. The thickness of the layer ejected in the ablation process amounted to 0.2–0.4 μm, while the remaining surface layer of thickness 0.2–0.3 μm contained fine inclusions of carbides and oxycarbides. With the thickness of the melted layer being 1–2 μm, defects were observed at a depth of more than 10 μm. After irradiation with a series of pulses ($N = 100$) had been completed, a redistribution of the elements was observed, which resulted in a change in the composition and in a refinement of the strengthening phases. Selection of a proper irradiation regime proved to be important here (this was especially true with respect to Φ and N). For instance, at $\Phi = 1$ J cm^{-2} per pulse, some alloys developed craters and surface cracks, which reduced the fatigue strength of the material. The researchers were able, by using a certain combination of Φ and N, to cure such defects and obtain processing regimes that substantially reduced the roughness of the blade surfaces (from 0.20–0.25 μm to 0.06–0.1 μm). This improved the quality of the surface, which is one of the main factors determining the corrosion resistance and erosion durability of the material. It was also discovered that thermal treatment at 300–600 °C after irradiation leads to annealing of defects and reduces residual tensile stresses, while the precipitates formed strengthen the material.

The above is corroborated by the fatigue curves that follow from the results of the tests. A number of such curves for the alloy VT18U are depicted in Fig. 21. With a broad range of loading cycles (10^6–10^9), the fatigue strength increases by 30–180%. Such processing also increases the corrosion resistance of samples in air by a factor of two to three and the resistance to salt attack in seawater by a factor of six to eight. Figure 22 depicts the test diagrams for three

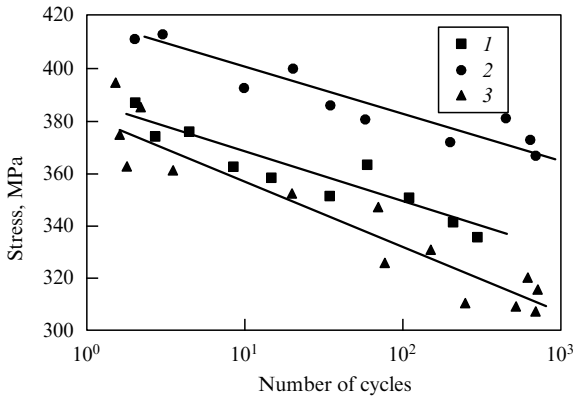

Figure 21. Fatigue curves for blades manufactured from the alloy VT18U after a run for 660 h on an engine at a load frequency of 3300 Hz and a temperature of 500 °C: *1*, initial state; *2*, after LHEB irradiation (140–150 A cm^{-2}, $N \geqslant 3$) and annealing (at 550 °C for two hours); and *3*, after LHEB irradiation without annealing.

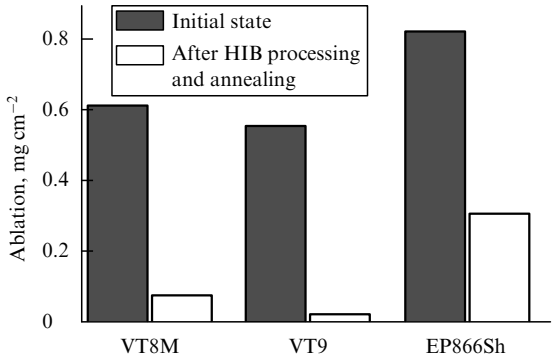

j, cm^{-2}	120–240	60–80	60–80
Number of pulses	3	3	3
T, °C	500	500	600
Number of cycles in seawater	150	150	200

Figure 22. Effect of processing with a high-power ion beam on the resistance to salt attack in seawater for EP866Sh steel and VT8M and VT9 titanium alloys.

groups of blades (70 blades per group): unprocessed, processed with HIB, and processed with HIB with subsequent annealing. Research has resulted in knowledge about the optimum regimes of irradiation and annealing for alloys of the following composition (in wt. %): EP866Sh (72 Fe, 16.5 Cr, 5.5 Co, 2.1 Ni, 1.6 Mo, 1.0 W, 0.6 Si, 0.3 Nb), VT8M (89.9 Ti, 5.9 Al, 3.7 Mo, 0.28 Si, 0.18 Fe), VT9 (86 Ti, 7 Al, 3.8 Mo, 2.5 Zr, 0.35 Si, 0.25 Fe), VT18U (Ti as base, 6.3 Al, 3.4 Mo, 0.2 Fe, 4.5 Zr, 1.5 Nb, 0.25 Si, 3.0 Sn). Hence, this technology has a promising future in the production of aircraft engines.

Recently a new application for HEB has been found, namely, the removal of nitrogen oxides from gas mixtures [156]. As a result of irradiating a mixture of NO (< 2 mol %) and N_2 with an HEB ($\leqslant 160$ keV, 700 ns, 2 A cm^{-2}, 12.6 ± 0.4 J cm^{-2} per pulse), a high effectiveness of removing NO was achieved (up to 1100 nmol J^{-1}). The results of such research could be used in metallurgy for removing residual gases in the process of high-purity metal melting and smelting.

9. Conclusion

In this review we have discussed a new and promising direction of development of solid state physics and radiation materials science, the effect of concentrated energy fluxes of high-power pulsed electron and ion beams on solid materials. Such beams generate superdense collective excitations of the electronic and atomic subsystems of solids. In the process of conversion of the energy of these excitations, unique structural and phase transitions occur, impossible in other types of action such as ion implantation and laser irradiation. The physics of high energy densities has developed a convenient mechanism for conducting fundamental studies in new areas, such as detection and investigation of the properties of a dense plasma; nonequilibrium phase transitions of the first and second orders that occur in high-power radiative, thermal, and mechanical fields; and computer simulation of processes in the tracks of heavy charged particles. The results of experiments facilitated the formation of new ideas concerning the physical nature of the interaction of high-power particle beams and matter. Some of these form the basis of new experimental methods of analysis, for instance, the diagnostics of the characteristics of strong radiation by the parameters of the generated ablation plasma.

The limited spectrum of properties of solid materials is the main reason why the progress in developing the technology of processing such materials is so slow. High-power beams ensure successful modification of the already existing properties and also create some new unique properties. A broad class of metals, alloys, and products manufactured from them has demonstrated real improvement in the operating characteristics, such as resistance to wear, fatigue strength under prolonged cyclic loads, and corrosion and erosion resistance. The improvement of these characteristics increases the reliability and service life of the products. Good results have been achieved by combining thermochemical methods, ion implantation, and intense irradiation. For instance, our preliminary studies in what is known as duplex treatment of Ti–V–Al alloys included preimplantation of ions of Fe and Zr on their surface and subsequent irradiation by a high-power electron beam [157]. We found that the microhardness and durability increase severalfold as a result of such treatment.

We predict a good future for some new resource-saving technologies, including preliminary doping of the surface layers of the processed materials with amorphous materials [71, 92], high-melting metals [101], and precious metals [92].

Special methods of deposition of ablation plasma have been used to produce thin films with good electrical, magnetic, and optical properties, high-hardness diamond coatings, and ultradisperse nanosized powders. We believe that in the near future this area of research will develop very fast.

The fairly high reproducibility of the experimental results combined with the productivity and effectiveness of the modification process and the fairly low production cost have stimulated the development of new methods of processing materials, with some of these methods finding their way into industrial technologies. This provides a satisfactory solution of some of the problems of radiation materials science, such as the fabrication of materials for nuclear power engineering,

the aerospace industry, mechanical engineering, microelectronics, etc. [158, 159]. Therefore in some cases HEB and HIB may be a good alternative to ion implantation and laser irradiation.

Here we have attempted to give a complete picture of all the relevant problems both from the scientific viewpoint and from the viewpoint of industrial applications. We base our reasoning on our investigations and on the studies done by highly acclaimed scientists in this field. The physics of the interaction of high-power beams and metals is treated, where possible, on the atomic, micro, and macro levels. The structural and phase transitions that cause the observed modifications of all the properties of solid materials have been analyzed on the basis of a unified concept of the transformation of the radiation energy in matter. This transformation depends on three main factors: (a) the type and parameters of the high-power beams of particles, (b) the initial characteristics of the matter, and (c) the parameters of the irradiation medium. By using certain combinations of these factors, the necessary modification can be achieved.

Today hit-or-miss (to a certain extent) experiments have been replaced by systematic investigations, and worldwide studies in this area are highly intensive, a fact corroborated by the reports presented at international conferences on the subject.

Notwithstanding the broad class of the materials being studied and the types and regimes of irradiation, it is still possible to classify the general features of the observed effects and processes:

(1) The observed effects and processes are determined by the collective excitation of the electronic and atomic subsystems of the solid.

(2) Most of these effects and processes are observed at intensities and fluences exceeding certain critical values (brittle fracture of solids under HEB, anomalous bulk strain hardening of metals irradiated with HIB, ablation of matter under irradiation, etc.).

(3) The features of these effects and processes are determined by the combined action of the generated intense radiation, thermal, and mechanical fields that cause essentially nonequilibrium phase transitions of the first and second orders to occur.

(4) They proceed at high rates, since the characteristic times of the important processes amount to $10^{-8}-10^{-5}$ s.

(5) They take place both in the irradiated region and in the unirradiated region, where in the latter region the observed long-range effects are related to the specific action of elastic, elastoplastic, and shock waves on the structure.

Recently in many areas of physics attention has been focused on long-range effects. Some of these effects represented in this review belong to structural and phase transitions of materials at large depths. Their existence is corroborated in the works of international research centers done for a broad class of materials and involving irradiation on many accelerators. Here, we believe, it is important (from the theoretical viewpoint) to separate the contributions of the radiation energy: the part that is spent for ablation, and the part that is spent for the generation of waves in the target. These processes are described by the same equations of propagation of waves but by a different equation of state for the plasma and the solid. An analytical description is hindered here by the absence of a satisfactory theory of nonequilibrium phase transitions that incorporates irradiation.

What are the main drawbacks of the work we have discussed in this review? If we compare the level of the experimental work with that of the theoretical interpretation, we will see that the physical picture of the observed phenomena is far from completion. Often, in developing various models, fairly crude assumptions are made, which often lead to substantial discrepancies between the experimental and theoretical results. And although the choice of the assumptions is justified fairly well, the problem is still there. We believe that there are several factors responsible for this situation.

First, the complexity, diversity, and interrelationship of phenomena that occur simultaneously, which substantially hinders the representation of these phenomena in the form of elementary actions and processes. Already at the first stage of interpreting these phenomena one must know the initial profile of the absorbed energy, which in all calculations is estimated by the total energy contribution of individual particles. For well-known reasons it is difficult to justify such an approach when high-power beams are involved.

Second, the uniqueness of these phenomena makes the choice of analogs and suitable models for their description extremely difficult.

Third, studies in this area have begun only recently and only at a few research centers.

The first two factors are very important.

In this review we limited ourselves to problems of the modification of properties of metallic materials. However, high-current electron beams are successfully used, say, to improve the electrical properties of insulators, to cut and crush hard-rock, to drive tunnels through rock mass, to sterilize medical instruments, and to treat water and food. This is additional proof of the importance of such studies and makes it necessary to find a broader interpretation of the results of these studies and a fast solution to the problems mentioned above.

We attempted to reflect the important trends in the given area of research, which has great potential both in the scientific aspects and in the accompanying new technologies. We expect that the interest in these problems will only grow in the future.

We are grateful to D Rej, B Wood, H Davis, K C Walter (Los Alamos National Lab.), T Renk, D Follstaedtt, J Knapp, R Buchett (Sandia National Lab.), R Stinnett (Quantum Manufacturing Technologies, USA), and K Yatsui (Nagaoka University of Technology, Japan) for sharing their scientific findings with us, for discussing separate results at seminars held at the respective laboratories, for fruitful discussions, and for critical remarks, which substantially enriched the content of the review. We are also grateful to D I Proskurovskiĭ, V P Rotshteĭn, and the staff of the Laboratory of Vacuum Electronics at the Institute of High-Current Electronics of the Russian Academy of Sciences (Tomsk) and to G E Remnev and V A Shulov for their help in conducting the experiments and for fruitful discussions.

This work was supported in part by the Ukrainian State Committee for Science and Technology (Raduga project No. 7.5.4/73-93 and project No. 005K/95).

References

1. Keldysh L V, in *Trudy Mezhd. Konf. po Fizike Poluprovodnikov* (Proc. Int. Conf. on Semicond. Phys.) (Moscow, 1968) p. 1307
2. Ashkinadze B M, Zinov'ev N N, Fishman I M *Zh. Eksp. Teor. Fiz.* **70** 678 (1976) [*Sov. Phys. JETP* **43** 349 (1976)]

3. Oswald R B *IEEE Trans. Nucl. Sci.* **NS-13** 63 (1966)
4. Steverding B et al. *J. Phys. D* **4** 54 (1971)
5. Steverding B et al. *J. Appl. Phys.* **43** 3217 (1972)
6. Avery R T, Keefe D *IEEE Trans. Nucl. Sci.* **NS-20** 1010 (1973)
7. Avery R T, Keefe D, in *Proc. Int. Conf.* "*Electron Beam Research and Technology*" *New Mexico, USA* Vol. 11 (1975) p. 61
8. Valyaev A N *Nucl. Instrum. Methods B* **141** 555 (1998)
9. Pogrebnjak A D, Rusimov Sh M *Phys. Lett. A* **120** 259 (1987)
10. Pogrebnjak A D et al. *Phys. Lett. A* **123** 410 (1987)
11. Nakagava Y et al. *Jpn. J. Appl. Phys.* **27** L719 (1988)
12. Nakagava Y et al. *Nucl. Instrum. Methods B* **39** 603 (1989)
13. Rej D J et al. *Nucl. Instrum. Methods B* **127/128** 987 (1997)
14. Itin V I et al., in *Fizika Iznosostoĭkosti Poverkhnosti Metallov* (Physics of Durability of Metal Surfaces) (Leningrad: Nauka, 1988) p. 119
15. Ivanov Yu F, Lykov, S. V., Rotshteĭn V P *Fiz. Khim. Obrab. Mater.* (5) 62 (1993)
16. Yatsui K et al., in *Proc. 10th Int. Conf.* "*High Power Particle Beams*" (San-Diego, USA, 1994) p. 27
17. Davis H A et al. *MRS Bulletin* **21** 58 (1996)
18. Davis H A et al. *Mater. Chem. Phys.* **54** 213 (1998)
19. Rudakov L I, Demidov V A, Uglov V S *Fiz. Khim. Obrab. Mater.* (4) 11 (1989)
20. Engelko V I, Lazarenko A V, Pechersky O P, in *Proc. 9th Int. Conf. High Power Particle Beams,Washington* Vol. 3 (1992) p. 1035
21. Proskurovsky D I et. al. *Vac. Sci. Tech. A* **16** 2480 (1998)
22. Itin V I et al., in *Proc. Int. Conf.* "*Energy Pulse and Particle Beams Modification of Materials*" *Dresden, 1989* Vol. 13 (Berlin: Phys. Res., 1990) p. 331
23. Steverding B, Lehning S H *J. Appl. Phys.* **42** 3231 (1971)
24. Steverding B, Lehning S H *J. Appl. Phys.* **45** 3507 (1974)
25. Boĭko V I et al. *Fiz. Khim. Obrab. Mater.* (1) 29 (1992)
26. Boĭko V I et al. *Fiz. Khim. Obrab. Mater.* (5) 28 (1993)
27. Boiko V I et. al. *Phys. Status Solidi A* **128** 369 (1991)
28. Akkerman A F et al. *Zh. Eksp. Teor. Fiz.* **89** 852 (1985) [*Sov. Phys. JETP* **62** 489 (1985)]
29. Shimotori Y et al. *J. Appl. Phys.* **63** 968 (1988)
30. Yatsui K et al. *Appl. Phys. Lett.* **67** 1214 (1995)
31. Shimotori Y, Yakayama M, Harada Sh *Appl. Phys.* **28** 469 (1988)
32. Yatsui K et al. *Phys. Plasmas* **1** 1730 (1994)
33. Remnev G E et al. *Pis'ma Zh. Tekh. Fiz.* **22** (4) 68 (1996) [*Tech. Phys. Lett.* **22** 336 (1996)]
34. Yatsui K et al., in *Proc. 11th Int. Conf.* "*High Power Particle Beams*" Vol. 1 (Prague, 1996) p. 262
35. Yatsui K *Laser Part. Beams* **7** 733 (1989)
36. Davis H A et al., in *Proc. 10th Int. Conf.* "*Ion Beam Modification of Materials*" (Albuquerque, 1996) p. 226
37. Gauter D S et al. *Mat. Res. Soc. Symp. Proc.* **279** 657 (1993)
38. Valyaev A N, in *Proc. Int. Conf.* "*Energy Pulse and Particle Beams Modification of Materials*" *Dresden, 1989* Vol. 13 (Berlin: Phys. Res., 1990) p. 558
39. Sudan R N, in *Inertial Confinement Fusion* (Eds A Caruso, E Singoni) (Int. School of Plasma Physics "Pierro Cardirolla" Varenna) (Bologna: Ital. Phys. Soc., 1989) p. 453
40. Van Devender J P *Plasma Phys. Controlled Fusion* **28** 841 (1986)
41. Rykalin N N (Ed.) *Vozdeĭstvie Kontsentrirovannykh Potokov Energii na Materialy* (Effect of Concentrated Energy Fluxes on Materials) (Moscow: Nauka, 1985)
42. Rykalin N N et al. *Lazernaya i Elektronno-Luchevaya Obrabotka Materialov. Spravochnik* (Laser and Electron Beam Material Processing: A Handbook) (Moscow: Mashinostroenie, 1985) [Translated into English (Moscow: Mir, 1988)]
43. Poate J M, Foti G, Jacobson D K (Eds) *Surface Modification and Alloying by Laser, Ion, and Electron Beams* (New York: Plenum Press, 1983) [Translated into Russian (Moscow: Mashinostroenie, 1987)]
44. Bykovskiĭ Yu A, Nevolin V N, Fominskiĭ V Yu *Ionnaya i Lazernaya Implantatsiya Metallicheskikh Materialov* (Ionic and Lazer Implantation of Metallic Materials) (Moscow: Energoatomizdat, 1991)
45. Donaldson E G *British Foundman F* **1540** 262 (1986)
46. Epifanov A S, Manenkov A A, Prokhorov A M *Zh. Eksp. Teor. Fiz.* **70** 728 (1976) [*Sov. Phys. JETP* **43** 377 (1976)]
47. Boĭko V I, Evstigneev V V *Vvedenie v Fiziku Vzaimodeĭstviya Sil'notochnykh Puchkov Chastits s Veshchestvom* (Introduction to the Interaction of High-Current Beams of Particles and Matter) (Moscow: Energoatomizdat, 1988)
48. Hewett C A et al. *Phys. Status Solidi A* **84** 49 (1984)
49. Ivanov Yu F et al. *Izv. Ross. Akad. Nauk Met.* **3** 140 (1993)
50. Ivanov Yu F et al. *Fiz. Met. Metalloved.* **75** (5) 103 (1993)
51. Ivanov Yu F et al. *Dokl. Akad. Nauk SSSR* **321** 1192 (1991) [*Sov. Phys. Doklady* **36** 874 (1991)]
52. Lykov S V et al. *Dokl. Akad. Nauk SSSR* **310** 858 (1990) [*Sov. Phys. Doklady* **35** 145 (1990)]
53. Markov A V, Proskurovskiĭ D I, Rotshteĭn V P, Preprint No. 17 of the Tomsk Science Center of the Siberian Division of the Russian Academy of Sciences (Tomsk: NTs SO RAN, 1993) p. 63
54. Zecca A et al. *Phys. Lett. A* **175** 433 (1993)
55. Fastow R, Mayer J W *J. Appl. Phys.* **61** 184 (1987)
56. Stinnett R W et al. *Mater. Res. Soc. Symp. Proc.* **316** 521 (1994)
57. Shulov V A *Pis'ma Zh. Tekh. Fiz.* **17** (9) 38 (1991) [*Sov. Tech. Phys. Lett.* **17** 621 (1991)]
58. Vaĭsburd D I et al. Inventor's Certificate No. 549046 MKI H01 L21/263 (Priority as of September 25, 1975)
59. Grace F I *J. Appl. Phys.* **40** 2649 (1969)
60. Bespalov V I et al., in *Sil'notochnye Impul'snye Elektronnye Puchki v Tekhnologii* (High-Current Pulsed Electron Beams in Engineering) (Novosibirsk: Nauka, 1983) p. 55
61. Baglin J E et al. *Appl. Phys. Lett.* **37** 187 (1980)
62. Pogrebnjak A D et al. *Phys. Lett. A* **241** 357 (1998)
63. Pogrebnyak A D et al. *Fiz. Khim. Obrab. Mater.* (1) 29 (1996)
64. Puska M V, Nieminen R *J. Phys. F* **12** 211 (1982)
65. Verigin A A, Kryuchkov Yu Yu, Pogrebnyak A D *Poverkhnost* **9** 106 (1988)
66. Pogrebnjak A D et al. *Phys. Status Solidi A* **123** 119 (1991)
67. Pogrebnjak A D et al. *Phys. Lett.* **141** 204 (1989)
68. Sahm P R, Sturm I S, in *Materials Sciences in Space*: *A Contribution to the Scientific Basis of Space Processing* (Eds B Feuerbacher, H Hamacher, R J Neumann) (Berlin: Springer, 1986) [Translated into Russian (Moscow: Mir, 1989) p. 143]
69. Valyaev A N, Pogrebnyak A D, Plotnikov S V *Radiatsionno-Mekhanicheskie Effecty v Tverdykh Telakh pri Obluchenii Vysokointensivnymi Impul'snymi Elektronnymi i Ionnymi Puchkami* (Radiative-Mechanical Effects in Solids Being Irradiated by High-Power Pulsed Electron and Ion Beams) (Alma-Ata: Gylym, 1998)
70. Pakk Y K et al. *Phys. Rev. B* **34** 823 (1986)
71. Pogrebnyak A D et al. *Izv. Vyssh. Uchebn. Zaved. Fiz.* **1** 52 (1987)
72. Mogilevsky M A *Phys. Rep.* **97** 357 (1986)
73. Murr L E, Gray G T, in *High Pressure Shock Compression of Solids* (Ed. J R Asay) (New-York: Springer, 1993) p. 187
74. Saarien K et al. *Phys. Rev. B* **39** 5287 (1989)
75. Pogrebnjak A D et al., in *Proc. Int. Conf.* "*Energy and Particle Beams Modification of Materials*" *Dresden, 1989* Vol. 13 (Berlin: Phys. Res., 1990) p. 308
76. Lavrent'ev V I, Pogrebnyak A D, Sandrik R *Pis'ma Zh. Eksp. Teor. Fiz.* **65** 618 (1997) [*JETP Lett.* **65** 651 (1997)]
77. Valyaev A N et al. *Pis'ma Zh. Tekh. Fiz.* **24** 47 (1998) [*Tech. Phys. Lett.* **24** 102 (1998)]
78. Pogrebnjak A D et al. *Surf. Coating Technol.* **111** 46 (1999)
79. Feldman L, Mayer J *Fundamentals of Surface and Thin Film Analysis* (New York: North-Holland, 1986) [Translated into Russian (Moscow: Mir, 1989) p. 207]
80. Didenko A N et al. *Phys. Status Solidi A* **89** 167 (1985)
81. Hirvonen J K, in *Ion Implantation* (Ed. J K Hirvonen) (New York: Academic Press, 1980) [Translated into Russian (Moscow: Metallurgiya, 1985) p. 391]
82. Kang X, Masugata K, Yatsui K *Laser Part. Beams* **13** 201 (1995)
83. Yanushkevich V A *Fiz. Khim. Obrab. Mater.* (5) 9 (1975)
84. Ivanov L I, Mezokh Z I, Yanushkevich V A *Fiz. Khim. Obrab. Mater.* (1) 38 (1977)
85. Ivanov L I, Yanushkevich V A, in *Fizika i Khimiya Plazmennykh Metallurgicheskikh Protsessov* (Physics and Chemistry of Plasma Metallurgical Processes) (Moscow: Nauka, 1985) p. 173
86. Yanushkevich V A et al. *Izv. Akad. Nauk SSSR Ser. Fiz.* **49** 1146 (1985)
87. Yanushkevich V A *Fiz. Khim. Obrab. Mater.* (2) 47 (1979)

88. Murr L E *Scr. Metall.* **12** 201 (1978)
89. Mogilevskiĭ M A, Th. D. Ph.-M. (Novosibirsk: IG SO AN SSSR, 1986)
90. Valyaev A N, Nazarov Yu K, Pogrebnjak A D, in *Proc. Int. Conf.* "*Ion Implantation and Ion Beam Equipment*" *Elenite, Bulgaria, 1990* (Singapore: World Scientific, 1990) p. 418
91. Zel'dovich Ya B, Raĭzer Yu P *Fizika Udarnykh Voln i Vysokotemperaturnykh Gidrodinamicheskikh Yavleniĭ* (Physics of Shock Waves and High-Temperature Hydrodynamic Phenomena) (Moscow: Nauka, 1966) [Translated into English (New York: Academic Press, 1967)]
92. Valyaev A N et al. Patent of Republic of Kazakhstan No. 4954, Bull. No. 3 (Priority as of August 15, 1997)
93. Renk T et al., Sandia Reports SAND-2101 (New Mexico: Sandia Natl. Lab, 1998); Renk T et al. *Phys. Plasmas* **5** 2144 (1998)
94. Russerguer T, Hallouin M *J. Appl. Phys.* **84** 1932 (1998)
95. Fastow R, Maron Y, Mayer J *Phys. Rev. B* **31** 893 (1985)
96. Bojarko Yu E et al. *Nucl. Instrum. Methods B* **17** 162 (1986)
97. Pogrebnjak A D, Remnev G E, Plotnikov S V *Mater. Sci. Eng. A* **115** 175 (1989)
98. Remnev G E, Shulov V A *Laser Part. Beams* **11** 707 (1993)
99. Koishibaev R G et al., in *Proc. 2nd Int. Conf.* "*Electron Beam Technol.*" (Varna, 1988) p. 751
100. Bannykh O A, Drits M E *Diagrammy Sostoyaniya Dvoĭnykh i Mnogokomponentnykh Sistem na Osnove Zheleza* Spravochnik (Phase Diagrams of Binary and Multicomponent Iron-Based Systems: A Handbook) (Moscow: Metallurgiya, 1986)
101. Pogrebnjak A D et al. *Surf. Coating Technol.* **99** 99 (1997)
102. Baturin A A et al. Preprint No. 21 of the Institute of High-Current Electronics of the Siberian Branch of the USSR Academy of Sciences (Tomsk: NTs SO AN SSSR, 1991)
103. Aleksandrov L E *Kinetika Kristallizatsii i Perekristallizatsii Tonkikh Plenok* (Kinetics of Thin-Film Crystallization and Recrystallization) (Moscow: Nauka, 1985)
104. Wood R E, Gilee G E *J. Thermal Transp. Melting* **23** 2923 (1987)
105. Krivobokov V P, Pashchenko O V *Zh. Tekh. Fiz.* **61** 188 (1991) [*Sov. Phys. Tech. Phys.* **36** 367 (1991)]
106. Pogrebnjak A D et al. *Nucl. Instrum. Methods B* **36** 286 (1988)
107. Pogrebnyak A D et al. *Metallofiz. Noveish. Tekhnol.* **19** 38 (1997)
108. Pfann W G *Zone Melting* (New York: Wiley, 1966) [Translated into Russian (Moscow: Mir, 1970)]
109. Belyuk S V et al., in *Proc. 2nd Int. Conf.* "*Electron Beam Technol.*" Vol. 3 (Varna, 1998) p. 595
110. Didenko A N, Krivobokov V P *Zh. Tekh. Fiz.* **58** 2002 (1988) [*Sov. Phys. Tech. Phys.* **33** 1214 (1988)]
111. Krivobokov V P, Pashchenko O V, Sapul'skaya G A *Zh. Tekh. Fiz.* **64** 37 (1994) [*Tech. Phys.* **39** 475 (1994)]
112. Asainov O Kh *Fiz. Khim. Obrab. Mater.* (2) 53 (1987)
113. Pogrebnjak A D *Phys. Status Solidi A* **117** 17 (1990)
114. Bataglin G et al. *J. Phys.* (Paris) **44** 209 (1983)
115. Bataglin G et al. *Thin Solid Films* **145** 147 (1986)
116. Bokshteĭn B E *Diffuziya v Metallakh* (Diffusion in Metals) (Moscow: Metallurgiya, 1978)
117. Gordeev A V, Rudakov L I *Zh. Eksp. Teor. Fiz.* **83** 2048 (1982) [*Sov. Phys. JETP* **56** 1186 (1982)]
118. Didenko A N et al. *Pis'ma Zh. Tekh. Fiz.* **13** 526 (1987) [*Sov. Tech. Phys. Lett.* **13** 217 (1987)]
119. Zhukov A V *Zh. Prikl. Mekh. Tekh. Fiz.* (5) 112 (1986)
120. Olemskoĭ A I, Pogrebnyak A D, Shul'zhenko V N *Izv. Vyssh. Uchebn. Zaved. Fiz.* (2) 110 (1993)
121. Landau L D, Lifshitz E M *Gidrodinamika* (Fluid Mechanics) (Moscow: Nauka, 1988) [Translated into English (Oxford: Pergamon Press, 1987)]
122. Chistyakov S A, Khalikov S V, Yalovets A P *Zh. Tekh. Fiz.* **63** 110 (1993) [*Tech. Phys.* **38** 5 (1993)]
123. Rej D I et. al. *Rev. Sci. Instrum.* **64** 2753 (1993)
124. Wood R W, Gilee G E *Phys. Rev.* **23** 2923 (1981)
125. Ballufi R V, King A G, in *Phase Transitions During Irradiation* (Ed. F V Nolfi, Jr) (New York: Applied Science Publ., 1983) [Translated into Russian (Moscow: Metallurgiya, 1989)]
126. Wilkins M L, in *Fundamental Methods in Hydrodynamics* (Eds B Adler et al.) (New York, 1964) [Translated into Russian (Moscow: Mir, 1967)]
127. Kononov B A, Stepanov Yu M, Yalovets A P *At. Energ.* **42** 326 (1977)
128. Chistjakov S A, Pogrebnjak A D, Remnev G E *Nucl. Instrum. Methods B* **42** 342 (1989)
129. Linlop W I *Appl. Phys. Lett.* **3** 210 (1963)
130. Isenov N R *Appl. Phys. Lett.* **4** 152 (1964)
131. Ehler A W *J. Appl. Phys.* **37** 4262 (1966)
132. Basov N G, Krokhin O G, Skliskov G V *IEEE J. Quantum Electron.* **QE-4** 988 (1968)
133. Hora H *Ann. Phys.* (Leipzig) **22** 402 (1969)
134. Hora H et. al. *Z. Naturforsch. A* **22** 278 (1967)
135. Yatsui K et al. *Laser Inter. Related Plasma Phen.* **10** 567 (1993)
136. Kang X, Katsuni K, Yatsui K *Jpn. J. Appl. Phys.* **33** Pt. 2 L1041 (1994)
137. Kang X, Masugata K, Yatsui K, in *Proc. 10th Int. Conf. Ion Beam Modification of Materials* (Albuquerque, USA, 1996) p. 244
138. Gauter D C et al. *Mater. Res. Soc. Symp. Proc.* **279** 657 (1993)
139. Rej D J et al., in *Proc. 9th Int. Conf. on High Power Particle Beams* (Washington, 1992) p. 34
140. Rej D J et al., in *Proc. 3rd Int. Conf. on Applications of Diamond Films and Related Materials* (Caithersburg, USA, 1995) p. 723
141. Siegel R W *MRS Bulletin* **15** 60 (1990)
142. Muller G, Schultheiss C, in *Proc. 10th Int. Conf. on High Power Particle Beams* (San-Diego, 1994) p. 833
143. Sonegawa T et al. *Appl. Phys. Lett.* **69** 1 (1996)
144. Kamihata S et al., in *Proc. 8th Int. Conf. on High Power Particle Beams* (Novosibirsk, 1990) p. 35
145. Dyer P E *Appl. Phys. Lett.* **55** 1630 (1989)
146. Olson J C et al. *Mater. Res. Soc. Symp. Proc.* **388** 171 (1996)
147. Remnev G E et al., in *Proc. 11th Int. Conf. on High Power Particle Beams* (Prague, 1996) p. 873
148. Rej D J et al. *J. Vac. Sci. Technol. A* **15** 1089 1997)
149. Kang X, Masugata K, Yatsui K *Jpn. J. Appl. Phys.* Pt. 2 **33** L1155 (1994)
150. Grigoriu C, Yatsui K, in *Proc. Symp. on Physics, Diagnostic Applications of Pulsed High Energy Density Plasma as an Extreme State* (Ed. K Isii) (Nagoya: Nat. Inst. Fusion Sci., 1996) p. 25
151. Melic C A et al. *J. Vac. Sci. Technol. A* **13** 1182 (1995)
152. Pogrebnjak A D, in *Proc. 10th Int. Conf. on High Power Particle Beams* (San-Diego, 1994) p. 232
153. Goncharenko I M et al. *Zashchita Metal.* **29** 932 (1993)
154. Shulov V A et al. *Surf. Coating Technol.* **99** 74 (1998)
155. Shulov V A, Nochovnaya N A, Remnev G E *Mater. Sci. Eng. A* **243** 290 (1998)
156. Nakagawa Y, Kawauchi H, in *Proc. 12th Int. Conf. on High Power Particle Beams* (Haifa, 1998) p. 7.22
157. Pogrebnjak A D et al. *Jpn. J. Appl. Phys.* **38** L248 (1999)
158. Regel' V R, Slutsker A I, Tomashevskiĭ E E *Kineticheskaya Priroda Prochnosti Tverdykh Tel* (Kinetic Nature of the Strength of Solids) (Moscow: Nauka, 1974)
159. Samsonidze G G, Trushin Yu V *Zh. Tekh. Fiz.* **58** 42 (1988) [*Sov. Phys. Tech. Phys.* **33** 24 (1988)]